15. SCANNING TRANSMISSION ELECTRON MICROSCOPY

J. M. COWLEY

1. INTRODUCTION

It was realized in the early days of electron microscopy [1] that the same electromagnetic, or electrostatic, lenses used in the conventional transmission electron microscopy (TEM) instruments could also be used to form a small electron probe by demagnifying a small bright source, and that probe could be scanned over the specimen in a two-dimensional raster. Scanning Electron Microscopy (or, Secondary Electron Microscopy) for the study of specimen morphologies and surface structure by the detection of low-energy secondary electrons, was widely developed in the 1950s, as was the microanalysis of specimens, with associated imaging, by detection of emitted X-ray. Scanning Transmission Electron Microscopy (STEM), making use of the electrons transmitted through a thin specimen, was developed more slowly. It was not until the 1970s that it was shown that STEM could compete with TEM in resolution and could have some important advantages (along with some disadvantages).

Albert Crewe realized that the way to produce an electron probe of very small diameter was to make use of a field emission gun (FEG) in which electrons are extracted from a cold, sharply-pointed metal tip by use of a high electrical field gradient. He and his associates built a small microscope column using electrons accelerated by 30 kilovolts and focused with a strong, short-focus electron lens to form a probe of diameter of approximately 0.4 nm [2]. The electrons scattered out of the incident beam cone were collected by use of an annular detector to form a dark-field image. With this arrangement, the first transmission electron microscope images of individual

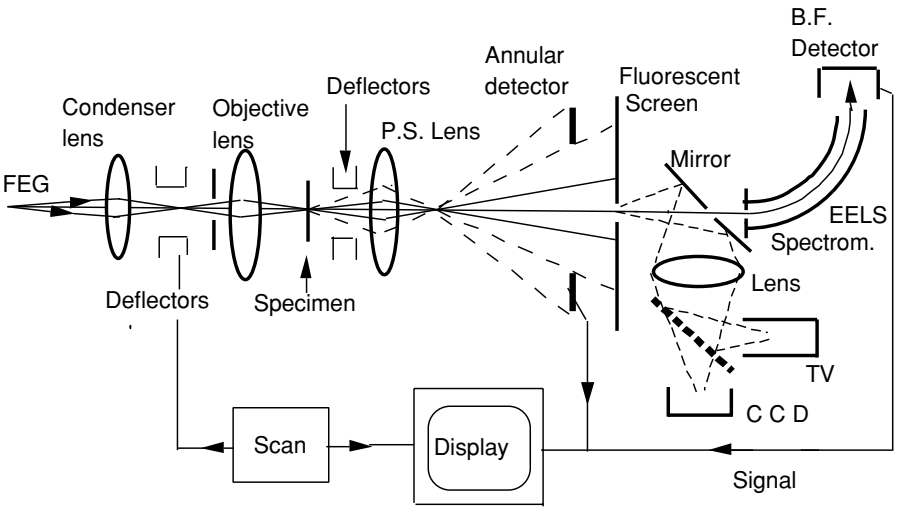

Figure 1. Diagram of a STEM instrument, modified for the convenient display and recording of shadow images and nanodiffraction patterns. A condenser lens and an objective lens produce the incident beam probe on the specimen and one (or more) post-specimen (P.S.) lenses govern the display of the diffraction pattern on a transmission phosphor screen which may be viewed using a TV-VCR system or a CCD camera with digital recording.

single heavy atoms, thorium atoms on a very thin amorphous carbon support, were recorded [3].

Successful applications to many areas of non-biological and biological science then followed rapidly. Several companies attempted to produce commercial STEM instruments. The only company to succeed in this was VG Microscopes, Ltd., of England which produced a succession of increasingly complicated instruments from about 1974 until their demise in 1997.

For STEM, the recording is essentially of a serial nature as the image signals are derived as the incident beam is scanned over the specimen, whereas in TEM the recording is in parallel with the whole image recorded simultaneously. One big advantage of STEM arises because, with the serial mode of recording, images formed with several different detectors may be recorded simultaneously. Bright-field and dark-field images and images with secondary radiations can be obtained during the same single scan of the incident beam over the specimen.

The principal components of a modified STEM instrument [4] are illustrated, diagrammatically, in Fig. 1. The source of electrons is a field-emission electron gun (FEG), preferably operating with a cold (i.e., room temperature) sharpened tungsten wire tip in ultra-high vacuum. A positive voltage, of about 3,000 volts with respect to the tip, creates a sufficiently high voltage gradient to draw the electrons out of the tip. The effective diameter of this very bright electron source is as small as 4 or 5 nm.

The field emission tip is held at a negative voltage of 100 to 300 kV. An earthed anode forms a weak electrostatic lens, which may be supplemented by the field of a weak electromagnetic lens, to form a narrow electron beam in the microscope column. The main lens producing the demagnification of the effective source, to form the small-diameter probe at the specimen level, is the objective lens, similar to the objective lenses used in TEM, with a high magnetic field and a focal length as small as 1 mm. One or more condenser lenses are placed before the objective lens in order to provide the flexibility in the beam parameters that are desirable for various modes of operation. Deflector coils, built into the bore of the objective lens, serve to scan the electron probe over the specimen.

For each position of the incident electron beam on the specimen, a diffraction pattern of the illuminated area is formed on a distant fluorescent screen. Since the beam focused by the objective lens is necessarily convergent, the pattern is a convergent-beam electron diffraction (CBED) pattern. Since the illuminated region of the specimen has a diameter approximately equal to the resolution limit of the images formed, usually less than 1 nm, the pattern is often referred to as an electron nano-diffraction (END) pattern. The scale of the diffraction pattern on the screen is affected by the weak post-specimen field of the objective lens and may be conveniently adjusted by means of one or more weak, post-specimen, magnetic lenses. The diffraction pattern may be observed and/or recorded by the use of a light-optical system consisting, for example, of a wide-aperture optical lens forming an image of the pattern in a low-light-level TV camera, coupled to a video-tape recorder (VCR), or else on a CCD camera for digital recording.

An aperture in the observation screen allows some part of the diffraction pattern, usually the central spot, to be transmitted into an electron energy-loss spectrometer (EELS), so that the EELS spectrum may be recorded or else an image may be made with electrons having any desired energy loss. The normal bright-field STEM image is obtained with the zero-loss electrons from the central beam of the pattern. Dark-field images may be obtained by selecting electrons that have lost the few electron volts associated with plasmon excitation, or with the many-electron-volt losses due to the inner-shell electron excitations characteristic of the various elements present. Dark-field images are also formed when any electrons scattered out of the incident beam cone are detected, with or without energy losses. Post-specimen deflection coils are used to direct any chosen part of the diffraction pattern to the entrance aperture of the spectrometer.

The most common form of dark-field imaging in STEM is given when all, or some selected part of the diffraction pattern, outside of the central beam spot, is detected, without energy analysis, by use of an annular detector. Crewe *et al.* [3] showed that the collection of the image signal in this way is much more efficient than for any of the dark-field TEM modes and led to interesting possibilities for signal manipulation.

Detectors may be placed close to the specimen to record the intensities of secondary radiations produced by the fast incident electron beam. Energy-sensitive X-ray detectors allow for the microanalysis of the illuminated specimen areas, or for the imaging of the specimen with the characteristic X-rays from particular elements. Low-energy

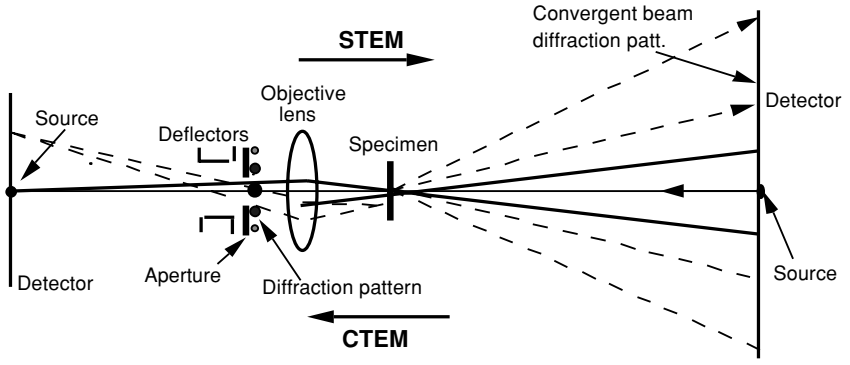

Figure 2. Diagram of the principal components of a STEM and a conventional TEM suggesting that, if the beam direction is reversed, the two imaging systems are equivalent, in accordance with the Reciprocity Relationship.

secondary electrons, or Auger electrons from specimen surfaces, may be detected and used to form secondary-electron (SEM) images of either the top side or the bottom side of the specimen.

Because the cold FEG must be operated in ultra-high vacuum, the whole microscope column, connected to the gun through a small aperture, should preferably be maintained at a high- (but not necessarily ultra-high-) vacuum. In the VG instruments, the column vacuum is normally better than 10^{-8} torr, an order of magnitude better than for most TEM instruments. This level of vacuum is attained only through the use of special techniques of construction of the column components, but has the advantage that the cleanliness of specimen surfaces may be maintained and the contamination of specimens under electron radiation may be kept to a minimum.

Initially, it was assumed that the contrast of STEM images could be interpreted in terms of an incoherent imaging theory, with the intensity at each point of the image given by the intensity of scattering from each irradiated point of the specimen. However, it was shown that the image intensities could be related to those of TEM by application of the Principle of Reciprocity [5, 6]. In the idealized case, it is stated that, for a scalar wave and elastic scattering, the amplitude of irradiation at a point B due to a point source at A, is the same as the amplitude at A due to a point source at B. Extending this to consider each point of a finite source and each point of a detector separately, one can confirm that the image given in a STEM system is the same as that for a TEM system, given the same components of lenses and apertures, but with the direction of propagation of the electrons reversed, as suggested in Fig. 2. Thus it has been demonstrated that the same variety of phase-contrast and amplitude-contrast modes as in TEM is possible in STEM, and the well-developed theory for TEM image contrast can be applied immediately for STEM imaging.

The commercially-provided STEM instruments used electrons accelerated by either 100 or 300 kV. In various laboratories, special instruments have been built in order to

exploit the advantages of using much higher or lower electron energies. Of the several projects to build million-volt instruments, the only one to produce useful results was that of Strojnik [7] who demonstrated the attainment of resolutions of about 1 nm at about 600 kV. As predicted, the high-voltage STEM gave much better imaging of very thick specimens than the contemporary high-voltage TEM instruments.

Medium-energy STEM instruments, operating at voltages of 5 to 20 kV, and used mostly in the reflection mode, have been built especially for surface studies in ultra-high vacuum [8–10]. Within the last few years, new TEM instruments with field-emission guns have become available commercially, and a flexibility of the electron optics allows them to be used for STEM imaging also. These so-called TEM/STEM instruments, operating at 200 or 300 kV, have been shown to produce excellent STEM images using the high-angle annular dark-field (HAADF) mode and also spectrometry and imaging with energy-loss electrons (EELS, and energy-loss imaging) [11–13]. It has not yet been demonstrated that such instruments have the same versatility in allowing the imaging, diffraction and microanalysis with the variety of modes possible with a dedicated STEM instrument, but their advent broadens the range of STEM instrumentation available at a time when the commercial manufacture of dedicated STEM instruments has temporarily ceased.

New experimental dedicated STEM instruments are now being tested. Some, incorporating aberration-corrector systems for the objective lenses and special monochromators, aim to provide resolutions of better than 0.1 nm [14, 15].

The STEM techniques clearly have many potential applications in the rapidly expanding field of nanotechnology. Many of the present and anticipated advances in this field involve the production and application of particles, tubes or wires, and interfacial assemblies for which the critical dimensions are of the order of one nanometer. The STEM instruments are ideally designed for the observation, characterization and analysis of materials having such dimensions. Adequate image contrast can be given by thicknesses of 1 nm with lateral resolutions of better than 0.2 nm. Compositions can be derived by microanalysis, and crystal structures can be recognized or determined from nanodiffraction patterns from regions having diameters of 1 nm or less. Special STEM techniques may be applied for the study of the structures of surfaces and the analysis of amorphous materials. Applications to the study of biological systems on a comparable scale are necessarily limited by radiation damage caused by the incident electron beam, but it has been shown that valuable data can be derived concerning the inorganic components of such systems. In this review, an account of the technical and theoretical bases for understanding STEM capabilities will be followed by examples of various applications that have been made to the study of samples relevant for future nanotechnology.

2. STEM IMAGING

The simplest form of imaging in a STEM instrument is shadow-imaging (or, point-projection imaging) in which a stationary incident beam is greatly defocused so that a small cross-over is formed well before, or after, the specimen, as suggested in the

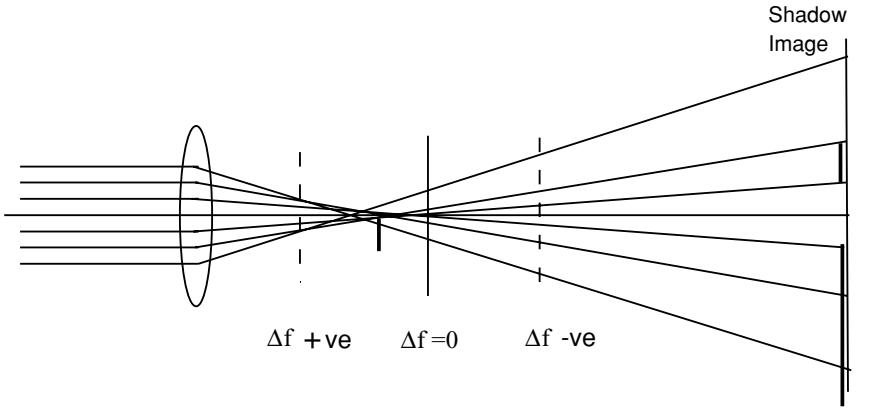

Figure 3. Diagram for the formation of shadow (point-projection) images for a lens having spherical aberration. If the cross-over comes before the specimen (over-focus) the image has positive magnification. If the cross-over comes after the specimen, the magnification is negative. For an object close to the paraxial focal point, there is infinite magnification for a particular radius in the image.

simple, geometric-optics diagram of Fig. 3. Images formed in this way are often useful for the initial survey of a specimen at low magnification, although it can be shown theoretically that the resolution attainable in this mode is given by the dimensions of the cross-over and is equal to that of the scanned STEM images. The magnification is positive or negative depending on whether the cross-over comes before or after the specimen [16].

When the cross-over is close to the specimen and the magnification becomes large, the image is distorted by the aberrations of the lens. When third-order spherical aberration is important, as for electromagnetic electron lenses, the image for a specimen placed close to the position of minimum diameter of the cross-over, as in Fig. 3, is greatly distorted. For incident paraxial rays, the cross-over is after the specimen so that for the central part of the image the magnification is high but negative. For rays making a large angle with the axis, the cross-over is before the specimen so that for the outer part of the image the magnification is high but positive. For one particular angle of incidence, the rays cross over at the specimen level so that the magnification becomes infinite. Taking into account the three-dimensional configuration of the rays, it can be seen that there is one radius in the image for infinite radial magnification and another radius for infinite circumferential magnification [17]. If the objective lens has astigmatism, the circular symmetery in the variations of magnification of the image is distorted. The image of a straight edge becomes a loop. This is in direct analogy with the "knife-edge test" of classical light optics.

More dramatic and useful effects appear if the specimen transmission is periodic. For a thin crystalline specimen, the shadow image of a set of parallel lattice planes, near focus, is distorted by the lens aberrations to give a set of loops, known as Ronchi-fringes in honor of Ronchi [18] who observed that such fringes are given when a

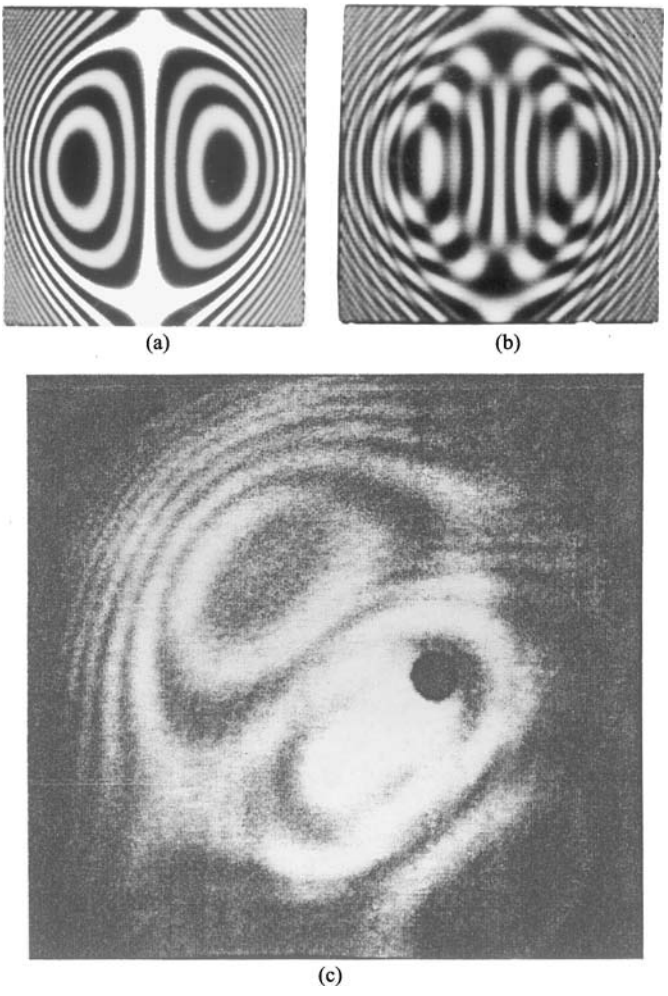

Figure 4. Ronchi fringes formed in the shadow image of a set of lattice planes in a crystal. (a,b) Simulated fringes for particular defocus values. (c) Observed fringes from the 0.34 nm periodicity of one side of a multi-wall carbon nanotube [136].

diffraction grating is placed near the focus of a large telescope mirror and showed that the fringes could be used to measure the lens aberrations. Typical Ronchi fringes in the electron shadow image of a crystal are shown in Fig. 4 [19, 12]. After the loops have been made symmetrical by careful correction of the astigmatism, measurement of their dimensions allows the accurate determination of the spherical aberration constant from a set of images obtained with known differences of defocus [20].

The circles of infinite magnification for general specimens, or the Ronchi fringes from crystalline specimens, also provide a convenient means for alignment of the

electron-optics of the microscope. These features of the shadow image allow the axis of the objective lens to be aligned with the detector aperture and provide a guide for the insertion of other apertures in the column.

The theoretical basis for STEM imaging may conveniently be referred to that for TEM imaging, making use of the Principle of Reciprocity. We show the equivalence for the simplest case.

The usual theory of electron microscope imaging is based on the Abbe theory for coherent radiation. For plane-parallel incident radiation, the transmission function for a thin object may be written, in one dimension for simplicity, $q(x)$. Then the bright-field image wave function for TEM is given by

$$\psi(x) = q(x) \otimes t(x) \equiv \int q(X) \cdot t(x - X) \cdot dX \tag{1}$$

and $t(x)$, is known as the Spread Function, which describes the loss of resolution due to the lens aberrations [21]. It is given by the Fourier transform of the lens transmission function, $T(u)$, where u is the angular variable, equal to $(2/\lambda) \cdot \sin(\phi/2)$, and ϕ is the angle of scattering. The convolution integral in (1), denoted by the $\otimes$ symbol, has the effect of smearing-out the $q(x)$ function. The image intensity is then given by the modulus squared of (1).

For STEM imaging, it is considered that a lens having a transfer function $T(u)$ forms a small probe for which the amplitude distribution is given by $t(x)$. The wave transmitted through the specimen when the probe is displaced by an amount X is then $q(x) \cdot t(x - X)$, and the intensity on the detector plane is given by the modulus squared of the Fourier transform, $Q(u) \otimes [T(u) \cdot \exp(2\pi i u X)]$. The signal collected to form the image is given by multiplying this intensity distribution by some detector function, $D(u)$, and integrating the transmitted intensity to give

$$I(X) = \int |Q(u) \otimes [T(u). \exp\{2\pi i u X\}]|^2 \cdot D(u).du \tag{2}$$

The form of $D(u)$, is related by Reciprocity to the TEM bright-field illumination. The equivalent of TEM with a plane-parallel wave incident, is the delta function detector, $\delta(u)$. For this case, (2) reduces to

$$I(X) = \left| \int Q(U) \cdot T(U) \cdot \exp\{2\pi i U X\} \cdot dU \right|^2 = |q(X) \otimes t(X)|^2 \tag{3}$$

which is the same result as for bright-field TEM, given above, since the STEM image is formed by recording the observed intensity as a function of the probe displacement, X.

The equation (2) may be used to determine the detected signal and the image contrast for other detector configurations, such as the cases where the detector is an aperture of finite diameter, or, with convenient approximations, for the dark-field

images for which the detector records the electrons scattered outside the incident beam cone. For this latter case, with an annular detector with a central aperture having a diameter slightly greater than the incident beam cone, a simple result is obtained if it is assumed that the intensity of the radiation scattered within the incident beam cone is proportional to the intensity scattered outside this cone. This assumption is good for the imaging of single isolated heavy atoms, but may fail if the specimen contains structure on a scale that will give diffraction maxima for scattering angles approximately equal to the half-angle of the incident cone, i.e., for structural details near the resolution limit of the microscope [22].

For this annular dark-field (ADF) mode, it is convenient to consider weakly-scattering objects and to write the transmission function as $q(x) = 1 + p(x)$, where $p(x)$ is much smaller than unity. Then it can be shown that, by taking $D(u) = 1$, and neglecting the scattering within the incident beam cone, the intensity of the image is given as $I(X) = |p(X)|^2 \otimes |t(X)|^2$. Thus the square of the scattering function is imaged with a resolution defined by the intensity distribution of the incident beam This result is interpreted as showing that the ADF contrast is given by "incoherent" imaging, in that the signal is proportional to the scattering power of the object with a spread function equal to the intensity distribution of the incident beam.

It may be noted that, if the amplitude distribution of the incident beam is assumed to be gaussian, the squaring of this gaussian gives an intensity distribution which is a gaussian with a width smaller by a factor of the square root of 2. Hence it may be concluded that dark-filed STEM gives a resolution better than that of bright-field TEM or STEM by a factor of about 1.4.

Application of the principle of reciprocity suggests that, with a finite detector diameter, rather than a delta-function detector as assumed in the derivation of (3), the resolution of the STEM bright-field image is degraded in the same way that the resolution in bright-field TEM is affected by applying a "damping function", or : "envelope function" to the phase-contrast transfer function, to take account of the illumination from a finite, incoherent source [21]. However, a simple argument indicates that, if the STEM detector has a diameter exactly equal to the diameter of the incident beam cone, the image signal, in the absence of absorption, is given by the total incident intensity minus the intensity in the annular dark-field image, and the image resolution of the bright-filed image should be the same as for the ADF image, although the contrast is necessarily lower [23].

On the basis of the simple incoherent imaging approximation to the contrast for the ADF STEM images, the contrast for single atoms should be approximately proportional to the square of Z, the atomic number. Hence heavy atoms could be distinguished clearly when held on a light-atom support. Also it was noted that for inelastic scattering the dependence on the atomic number is different so that, if the inelastically scattered electrons could be detected by use of an energy-loss spectrometer, the ratio of the signals recorded simultaneously from the elastically and inelastically scattered electrons would give image contrast proportional to some power of the atomic number and independent of the number of atoms present. This provided a further means for separating the signals from heavy and light atoms.

A further valuable form of dark-field STEM imaging makes use of an annular detector having a large inner diameter so that it detects only those electrons scattered to relatively high angles, usually of 50mrad or more for 100keV electrons. It was pointed out by Howie [24], that in ADF images of heavy-atoms on light-atom materials, such as metal particles in light-atoms catalyst supports, confusion could arise from strong signals given by small crystalline regions of the supports. This trouble could be avoided by noting that the diffraction spots from crystals extend to only limited scattering angles. By use of a high-angle annular dark-field (HAADF) detector, these contributions could be avoided. It was realized that the scattering to higher angles was mostly thermal diffuse scattering, due to the atomic vibrations. While the elastic crystalline reflection intensities fall off with scattering angle approximately in proportion to $f^2(u)$, the square of the atomic scattering factor, the intensity for first-order thermal diffuse scattering is proportional to $u^2 f^2(u)$, and so peaks at higher angles [25]. For thick specimens, the higher-order thermal diffuse scattering can become important and this peaks at even higher angles [26].

As a first approximation, it may be assumed that, as in the case of first-order thermal diffuse scattering, the HAADF signal may be assumed to be proportional to the square of the atomic number of the elements present. More complicated dependencies are appropriate when multiple diffuse scattering is present or in the case of crystalline specimens, to be considered later.

A further useful form of dark-field STEM imaging is given by the use of a thin annular detector, in which the outer and inner diameters of the detector differ by as little as 10 percent, so that only those electrons scattered within a limited range of angles are detected. The effective mean radius of the thin annular detector may be selected by varying the strengths of the post-specimen lenses to vary the magnification of the diffraction pattern on the detector plane. Then this thin-annular-detector dark-field (TADDF) mode may be useful in some cases, for imaging particular components of a compound specimen [27, 28] as in the case illustrated in Fig. 5.

In particular, it has been shown that the TADDF mode can be useful in the preferential imaging of nanocrystalline or amorphous phases in a composite specimen when the components have maxima of their scattering intensities for different scattering angles. For example, nanocrystals of carbon in a layer 1 nm thick could be readily distinguished from a supporting film of amorphous silica, 6 nm thick, when the thin annular detector was set to collect the scattering to the strong carbon peak, corresponding to a d-spacing of about 0.34 nm, which is well separated from the main peaks of the scattering intensity from the amorphous silica [29].

Further interesting imaging modes are given when the post-specimen lenses are used to enlarge the diffraction pattern until the central beam spot is comparable in diameter with the inner diameter of the annular detector. If the incident beam spot is just slightly smaller the inner detector diameter, bright image contrast is given when a rapid variation of the specimen thickness or scattering strength acts like a prism to deflect the incident beam. This so-called "marginal" imaging mode then shows the locations of edges, or any sudden variation of the scattering power of the specimen.

If the central beam spot is made slightly larger than the inner diameter of the annular detector, a bright-field image is produced. An analysis of this mode suggests that the

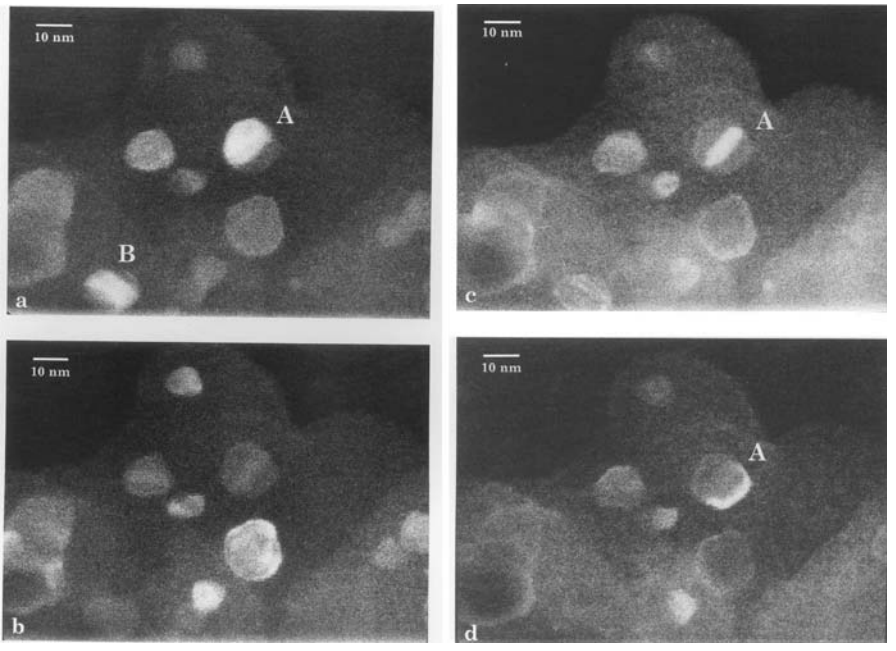

Figure 5. STEM images of a specimen of nanocrystals of Pt in amorphous carbon using a thin annular detector with average detection angles corresponding to d-values of (a) 0.056 nm, (b) 0.076 nm, (c) 0.098 nm and (d) 0.120 nm. For (c), the scattering from the a–C is strong [27].

resolution of this bright-field image should be better than that of the normal, axial bright-field STEM image by a factor of about 1.7 [28]. Application of the reciprocity principle suggests that this mode of bright-field STEM imaging with a thin annular detector should be equivalent to the bright-field TEM imaging mode in which the specimen is illuminated by a hollow cone of incident electrons, or else, more conveniently, the incident beam is tilted to a fixed angle and then gyrated so that the integration over time is equivalent to the hollow-cone illumination [30]. For similar geometries, this hollow-cone TEM mode should show the same properties as the TADDF STEM in dark-field and the same improvement of resolution for bright-field images. For practical applications, the TADDF STEM mode is probably more simple, experimentally, and more convenient.

Detectors of non-circular symmetry, including those with two separate halves or four individual quadrants, have been employed for high-resolution, differential phase contrast and the detection of weak magnetic fields [31].

3. STEM IMAGING OF CRYSTALS

3.1. Very Thin Crystals

When the specimen is a very thin crystal with the incident beam direction close to a principal crystal axis, the diffraction pattern on the detector plane is a regular array

of diffraction spots with separations inversely proportional to the dimensions of the projected unit cell of the crystal. Because, in STEM, the incident beam is convergent, each diffraction spot is spread out to form a circular disk of the same diameter as the incident beam disk. Provided that the crystal region illuminated is very thin, the intensity distribution across each diffracted beam disk is uniform. For increasing thicknesses, the diffraction disks are crossed by dark or bright lines, corresponding the variations of diffracted beam intensities as the incident beam orientations varies, as in the convergent-beam electron diffraction (CBED) patterns commonly observed in TEM instruments. For relatively very thick crystals, as in CBED, a diffuse background, arising from inelastic scattering processes, accumulates, crossed by dark and light Kikuchi lines.

In STEM instruments, the illuminated area of the specimen is normally 1 nm or less in diameter and the incident beam cone may be considered as completely coherent. For CBED in TEM instruments, the area of the specimen illuminated normally has a diameter of about 100 nm, and, to a good approximation, the incident beam may be assumed to be completely incoherent. It has been shown that, for the elastic scattering from a perfect crystal, without defects or boundaries, the diffraction intensities are exactly the same for the coherent and incoherent cases [32]. Hence, the diffraction patterns observed in a STEM instrument may be used for all of the many applications developed for the CBED technique using TEM instruments [32, 33].

When the cone angle for the incident beam in STEM is so large that the diffraction spots overlap, or when there are defects or boundaries in the crystal region illuminated, giving rise to scattering between the perfect-crystal diffraction spots, there can be coherent interaction between electron waves scattered into the same direction, but coming from different directions within the incident beam cone. These coherent interactions give rise to some striking interference effects. Interpretation of the "coherent CBED" observations can provide important additional information about the specimen structure and allow interpretation of STEM images of crystals and their defects.

The condition that diffraction spot disks should overlap appreciably is the condition that the incident beam should have a diameter smaller than the periodicity in the crystal corresponding to the diffraction spot separation. Then electron waves coming from different directions within the incident beam cone can give diffracted beams in the same direction for the two different reflections, as suggested in Fig. 6. These two coincident diffracted beams then interfere, and a set of fringes appears in the region of overlap of the spots. The positions of the fringes depend on the relative phases of the two reflections. This is the basis of the suggestion that the coherent CBED patterns should give the solution to the "phase problem" of X-ray diffraction (and kinematical electron diffraction) in that the observation of the regions of overlap of all the pairs of diffraction disks in a two-dimensional diffraction pattern would supply the information on the relative phases of the reflections, needed for the unambiguous determination of the projected crystal structure [34–36]. This is the basis for the proposed technique of ptychography for crystal structure analysis.

However, the relative phases of the diffracted beams depend on the position of the incident beam relative to the origin of the unit cell. As a beam is translated across

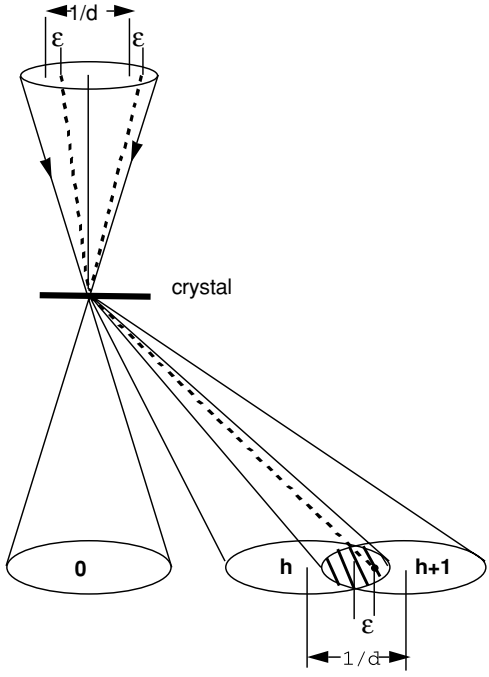

Figure 6. Diagram to suggest the interference of rays from different parts of a coherent source to give interference fringes in the region of overlap of adjacent orders of reflection from a thin crystal.

the crystal, the interference fringes in the areas of overlap of the diffraction spots are seen to move. These movements of the fringes provide a basis for interpreting lattice fringes in STEM images. If a small detector is placed in the region of overlap of two diffraction spots, it will record a sinusoidally-varying signal as the incident beam is translated, so that the image will show fringes having the periodicity of the crystal lattice [36].

If the incident beam cone is further enlarged, until the diffraction spot disks from many reflections overlap at the origin of the diffraction pattern, the image formed with a small axial detector is given by the coherent sum of all the diffraction beam amplitudes, and the image shows the periodic structure revealing the distribution of the scattering matter within the unit cell. Such an incident beam cone size corresponds to an incident beam diameter much smaller than the crystal periodicity, and the image resembles that for HRTEM with an objective aperture large enough to include the corresponding number of diffracted beams [37].

The reciprocity relationship allows the STEM images of thin single crystals to be understood and calculated by the standard methods used for TEM. For larger crystal thicknesses, especially when the inelastic contributions to the image begin to become important, the differences between the STEM and TEM cases may become significant.

3.2. Dynamical Diffraction Effects

For all crystals except those composed of light atoms and no more than a few nanometers thick, dynamical diffraction effects (coherent multiple scattering) are significant and dominate the scattering for most experimental cases, especially when heavy atoms are present [21]. For a crystal of gold in [100] orientation with 100 keV electrons, for example, the diffracted beams attain the same intensity as the incident beam for a thickness of about 2 nm, and the incident and diffracted beam intensities oscillate with thickness increase, almost sinusoidally, with a periodicity of about 4 nm.

In the presence of strong dynamical scattering, there is no intuitively obvious connection between the diffraction pattern or image contrast with the projection of the structure of the crystal. Various schemes have been proposed whereby the atom arrangement can be derived from the observed intensities of series of diffraction patterns or images [38, 39] but these have not led to practical routine procedures. The only practical procedure at present is the established trial-and-error method of postulating a structure and then calculating the image or diffraction pattern by use of one of the computer programs, based on either the multislice approach [40–42] or on the Bloch-wave method, or scattering matrix multiplication method, derived from the Bethe theory [43–45]. Accounts of these computing techniques are given, for example, in references [32, 46, 47].

In order to calculate the dynamical diffraction effects in STEM diffraction patterns or bright-field images, one could, in principle, take the square of the sum of the amplitudes calculated for each incident beam direction within the incident beam cone, added coherently with the correct phase relations, for each incident beam position. Alternatively, one could take, as the input to a multislice calculation, the amplitude distribution of the focused incident beam. Since this distribution is essentially non-periodic, it is then necessary to use the periodic-continuation approximation, assuming a periodic array of incident beams at the origin points of a very large unit cell, with many times the dimensions of the projected crystal unit cell. However, the large amount of computing involved in these approaches may often be avoided by making the calculation for the reciprocity-related TEM conditions, for which a single multislice or Bethe-type calculation may suffice. Calculations that involve inelastic scattering into a continuous diffuse background of the diffraction pattern are necessarily more complicated and tedious [48].

For ADF STEM images, the simple incoherent imaging approximation given above, with image intensity proportional to the square of the projected potential function, fails in the presence of dynamical scattering. The image intensities may be calculated by summing the computed intensities of the diffraction pattern, outside of the central beam spot, obtained for each position of the incident beam. For HAADF imaging it may usually be assumed that the image intensity is proportional to the thermal diffuse scattering (TDS) intensity. Since the integration is made over a wide range of scattering angles and all scattering directions, the assumption of incoherent scattering from individual atoms may be made. For single-scattering TDS, the assumption may be made of a simple TDS form factor for each atom, dependent on the atomic number,

the temperature and the atom environment. An extension of such an assumption to include the possibility of multiple TDS scattering, is feasible [49].

3.3. Channeling

For the observation of electron diffraction patterns and the high-resolution imaging of crystals, it is often of interest to consider the special case in which the incident beam is parallel to one of the principle axes of the crystal structure. Then the incident electrons are directed along the rows of closely-spaced atoms, and the channeling phenomenon is observed. The projected potential of the crystal may be considered to have deep wells at the atomic positions and the electrons may be thought of as trapped within the potential wells, giving rise to special transmission effects. As in the case of electrons bound to the three-dimensional potential wells of atoms in normal quantum theory, it may be considered that the electrons in the two-dimensional fields of the atom rows may have bound *1s*, *2s*, *2p*, etc states, with the *1s* states usually predominating.

Treatments along these lines were first introduced with plane waves incident, to describe the diffraction and imaging in HRTEM [50]. Related treatments for the STEM case of incident focused beam probes followed [51]. It has been shown that for an incident conical STEM beam with its axis aligned with a row of atoms through a crystal, in the absence of absorption, the intensity along a line through the centers of the atoms varies periodically with distance into the crystal. The width of the beam is a minimum when the intensity on the central line is a maximum. For a crystal of gold in [100] orientation, for example, the beam diameter may periodically become as small as 0.03 nm, or as large as 0.1 nm. The periodicity of this variation in the beam direction is about 5 nm [52]. For graphitic carbon, this periodicity is as great as 60 nm and the minimum beam diameter is about 0.06 nm [53]. In the presence of absorption, the oscillations of the beam intensity are damped for increasing beam paths.

This is the "atomic focuser" effect. A single heavy atom, or a row of atoms extending through a thin crystal, may be thought of as constituting an electrostatic lens for electrons, providing a focused beam with a diameter of 0.05 nm or less at the exit face. The effective focal length of such a lens is about 2 nm [54]. It has been suggested that such fine probes may form the basis for a STEM imaging scheme giving resolutions of 0.05 nm or better. Alternatively, the periodic arrays of such probes created when a plane wave is transmitted through a thin crystal in an axial direction, may form the basis for new methods for STEM or TEM imaging with comparable resolution [55, 56]. Preliminary experiments with specially favorable configurations [53] and computer simulations [57] have confirmed these possibilities.

4. DIFFRACTION IN STEM INSTRUMENTS

4.1. Scanning Mode Electron Diffraction

In the early commercial STEM instruments, provision was made for the serial recording of diffraction patterns. Post-specimen deflector coils, the so-called Grigson coils, are

used to scan the diffraction pattern over a detector aperture, which may be the entrance aperture to the energy-loss spectrometer. The signal from the elastically or inelastically scattered electrons can be recorded or can give a display of the diffraction pattern intensities on the cathode ray screen. An important advantage over the TEM SAED mode is that the diffraction pattern may come from a much smaller specimen area, of diameter equal to that of the incident beam probe.

The principle practical limitations of this mode arise because of the inefficiency in the detection system. Only a very small fraction of the diffraction pattern is recorded at a time. The small area of the specimen giving the pattern is being irradiated by the incident beam during the rather extended recording time and no image of the specimen is available during this time. The effects of specimen drift and irradiation damage may be important.

4.2. Two-Dimensional Recording Systems

The diffraction pattern formed for any position of the incident beam on the specimen may be observed on a fluorescent screen, as suggested in Figure 1. The pattern may be viewed and recorded using a low-light-level television camera, coupled with a video-cassette recorder (VCR), or else using a CCD camera with an associated digital image recording system. With the field-emission gun and normal lens settings, sufficient intensity is available to allow diffraction patterns to be recorded with the TV-VCR system, at the TV rates of 30 patterns per second. With the CCD, the digital recording is more quantitative and more sensitive to small signals, but the recording is slower, with normally only a few frames per second.

In a configuration equivalent, by reciprocity, to the SAED mode in TEM, the condenser lens may be focused to form a cross-over just before the objective lens so that the objective lens forms a parallel beam at the specimen, giving a sharply-focused diffraction pattern on the observation screen. The diameter of the illuminated region of the specimen can be as small as a few tens of nm, and is given by the reduced image of the aperture placed in what, for TEM, would be the image plane of the objective lens. This configuration has been used effectively for quantitative diffraction by Zuo *et al.* [58].

When the incident beam is focused on the specimen, the diffraction patterns are necessarily convergent beam patterns, with spot sizes inversely proportional to the width of the incident beam. For the minimum beam dimensions at the specimen level of about 0.2 nm, the diffraction patterns spots are so large that they overlap for most crystals. These conditions are valuable for special purposes when coherent interference effects are being observed, but for most practical investigations of local structure, it is convenient to use an incident beam of larger diameter, of the order of 1 nm, and the higher intensity obtained by suitable settings of the condenser lenses. Figure 7, for example, shows some diffraction patterns obtained with a beam probe of diameter about 0.7 nm in diameter, for which the diffraction spots are well separated for most crystals having unit cell dimensions no greater than about 1 nm. Such electron nanodiffraction (END) patterns may usually be interpreted in

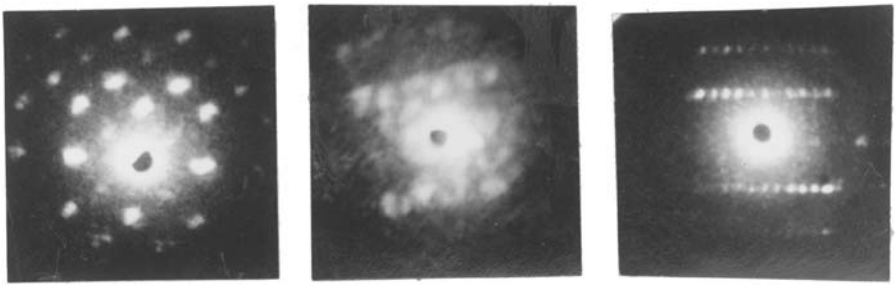

Figure 7. Nanodiffraction patterns obtained with a focussed incident beam of diameter 0.7 nm from the iron-containing cores of ferritin molecules. (a) A magnetite-like phase in [100] orientation. (b) The hexagonal phase in [110] orientation showing the lines of spots corresponding to the 0.94 nm spacing. (c) As for (b), but with the beam defocused to give smaller spot sizes [59].

the same way as parallel-beam diffraction patterns except that the diffraction spots are larger. They have proven useful for the study of many nanocrystalline materials, the localized defects in larger crystals, and the local ordering in quasi-amorphous materials.

For those specimens having lattice plane spacings so great that the diffraction spots in the END patterns overlap, it is often convenient to make the beam diameter at the specimen larger by defocusing the objective lens. Then the spot sizes for small crystals are governed more by the crystallite sizes than by the beam convergence, and the close rows of spots may be separated, as shown in Figure 7, (b) and (c) [59].

4.3. Convergent-Beam Electron Diffraction

In TEM instruments, the CBED method has many valuable applications, depending, for the most part on the observations and measurements of dynamical diffraction effects. The applications include the determination of lattice parameters and thicknesses of crystals, the determinations of space-group symmetries without the normal limitations of kinematical diffraction, the highly accurate measurement of electron scattering amplitudes and the consequent determination of the potential, and electron-density, distributions in relatively simple crystals [33, 60].

For CBED in a normal TEM instrument, without a field-emission gun (FEG), the diameter of the region giving the CBED pattern is usually 20 to 100 nm. In a STEM instrument, or in a TEM/STEM instrument, with a field emission gun as a source, CBED patterns may be recorded with a beam cross-over at the specimen having a diameter approximately equal to the resolution limit for dark-field images, which may be as small as 0.2 nm.

The CBED patterns obtained with a STEM instrument may be used for all the same purposes as CBED in TEM instruments, but with the added advantage that the

perfect-crystal regions studied may be much smaller. However, to date, very little has been done to take advantage of these possibilities, presumably because the equipment for making accurate intensity measurements, including CCD detectors or image plates, has not been installed in STEM instruments and other instrumental factors have not received the same amount of attention.

4.4. Coherent Nanodiffraction

A number of interesting and potentially useful effects have been observed in nanodiffraction patterns obtained from crystal specimens containing discontinuities. A planar discontinuity, parallel to the incident beam, for example, gives a continuous streak, perpendicular to the discontinuity, in kinematical diffraction patterns. But for a coherent convergent incident beam, there can be interference between the electrons scattered in neighboring directions. The circular disks of the spots given by the perfect crystal may be modulated so that bright arcs appear on the edges of the disks separated along the line perpendicular to the discontinuity. For example, with the incident beam illuminating the edge of a small gold crystal or a cube-shaped crystallite of MgO, the diffraction spots appear to be split into two arcs [61]. It was shown by Cowley and Spence [61] that such a splitting is to be expected from the interference of the electron waves from the two sides of the discontinuity.

For diffraction from the edges of a small crystal, the amount and form of the modulation of the diffraction spots is dependent on the lateral extent of the edge and the form of the edge; whether there is a flat face parallel to the beam or whether the beam cuts across the top of a pyramid or wedge of crystal. In some cases, the complete circumference of the circular diffraction spot may have enhanced intensity, so that the spots become rings [62]. In principle, it should be possible to derive the complete three-dimensional geometry of a crystallite by observing the form of the diffraction spots obtained from each of its edges.

Similar spot splittings or distortions may be observed for some of the diffraction spots when there is an internal boundary between two regions of different structure within a crystal. For crystals of binary alloys having long-range ordering, nanodiffraction from the regions of out-of-phase domain boundaries, show a splitting of the "superlattice reflections", but not of the "fundamental" reflections. By observing the form of the splitting it is possible to derive the form of the boundary [63, 64].

Similarly, in face-centered cubic metals, where twinning occurs on {111} planes, if the incident beam is parallel to a twin plane, some reflections are not affected by the twinning and so the diffraction spots are not affected, but for other reflections the crystal periodicity shows a discontinuity so that the diffraction spots are split [65]. From such observations, the nature of any discontinuity can be deduced.

When a large aperture, or no aperture, is used in the STEM instrument, a perfect thin crystal gives the pattern of Ronchi fringes, as described above. The perturbation of the Ronchi pattern in the presence of a discontinuity in the crystal structure is profound and may, in principle, be analysed to deduce the nature of the discontinuity. However, the possibility of such analyses has been very little explored.

5. MICROANALYSIS IN STEM

5.1. Electron Energy Loss Spectroscopy and Imaging

It was realized, from the beginning [2], that it is easy and useful to attach electron spectrometers to STEM instruments so that images may be formed with electrons that have lost energy through inelastic scattering processes, and energy-loss spectra may be obtained to allow compositional analysis of very small regions of the specimen. Use of the field emission guns allowed ample signal strength for the analytical data and imaging by EELS or X-ray emission with spatial resolutions small as 1 nm [66]. It may be noted that these techniques form valuable adjuncts for other applications of STEM instruments especially because they are readily available and their access does not hinder the use of any of the STEM imaging or diffraction modes.

Bulk plasmon losses, due to the collective excitations of nearly-free electrons in the interior of solids, ranging from a few volts up to about 50 eV, may give strong characteristic peaks in the energy-loss spectrum, and provide information of modifications of nearly-free electron states in solids due to variations of composition or bonding [67]. These excitations are generally considered not to be highly localized, but experimental results have indicated that they can show changes in the electron energy states over distances as small as 1 nm [68].

5.2. Secondary Emissions

In addition to the emission of X-rays, characteristic of the elements present in the sample, the incident high-energy electron beam gives rise to the emission of low-energy secondary electrons with energies of a few eV, and the Auger electrons, with energies of tens or hundreds of eV, produced when the energy from the excited inner shells of atomic electrons is transferred to produce the emission of outer-shell electrons. Because these low-energy electrons have very limited path-lengths in solids, the images created by detecting them comes from the thin surface layers of solids. Dedicated instruments designed for secondary electron microscopy (SEM) or Auger electron microscopy (AEM) have long been used for the study of surface structure and morphology. The spectroscopy of Auger electrons (AES), provides the means for the analysis of the chemical composition of surface layers. The advantage of STEM instruments for SEM or AEM imaging or for AES is that the spatial resolution may be high, of the order of 1 nm or better. Several authors have determined that the spatial resolution is not degraded by delocalization of the process of exciting the electron emission [68].

The specimen in a STEM instrument is usually immersed in the strong magnetic field of the objective lens. The low-energy electrons emitted from the specimen travel in spirals around the lines of force of the magnetic field. When they exit the field, they may be deflected into a detector or else into a spectrometer so that their energy distribution may be analysed. For the thin specimens studied in STEM instruments, low energy electrons are emitted from both the top and bottom surfaces and, in specially-designed instruments, images or analyses of both surfaces may be obtained simultaneously, and compared with the images or analyses produced by the transmission of the incident fast electrons [69].

6. STUDIES OF NANOPARTICLES AND NANOTUBES

6.1. Nanoparticles

The STEM techniques have obvious relevance for the rapid increase of scientific and industrial interest in the formation and properties of small particles having diameters of the order of one, or a few, nanometers. Such particles can be imaged preferentially by use of special STEM imaging modes. Their crystalline structures can be determined by nanodiffraction and their compositions can be determined by microanalysis with high spatial resolution.

Studies of supported metal catalysts have proved valuable. For dispersions of nanometer-size platinum particles on supports of alumina or other oxides, nanodiffraction from individual particles chosen from STEM images, has revealed their structures and the presence of twinning. In some cases it has been shown that the oxides of platinum may be present [70].

For gold-ruthenium catalysts particles on a support of magnesia, one unexpected finding was the presence of ruthenium in a body-centered cubic modification instead of the usual hexagonal structure [71]. This finding is consistent with the increasing evidence that nanometer-size metal particles may often have structures other than those stable in bulk.

Small particles, particularly of noble metals, are frequently found to be twinned, or multiply twinned [72]. Gold particles with diameters from 10 to 100 nm take the form of decahedra, with five tetrahedrally-shaped regions of perfect crystal related by twinning on (111) planes, or of icosahedra with twenty mutually twinned regions. The evidence from TEM is inconclusive for particles smaller than 10 nm. Nanodiffraction from a sample of gold particles on a polyester support showed that some particles of sizes 3 to 5 nm had multiple twinning of this type, but smaller particles were mostly untwinned [73].

Some minerals are found only in microcrystalline form and the determinations of their structures by conventional X-ray or electron diffraction methods are difficult. The mineral ferrihydrite, for example, occurs in two forms. The "six-line" form, 6LFh, gives X-ray powder patterns with only six diffuse lines. Patterns from "two-line" form, 2LFh, contain only two very diffuse lines. A hexagonal crystal structure has been proposed for the 6LFh, [74]. but only guesses are available for the 2LFh. Nanodiffraction has provided single-crystal patterns from nanosized particles of both types of material, allowing their crystal structures to be determined and refined. In both cases, the material was found to consist of a mixture of crystallites of several phases [75, 76]. The 6LFh samples, for example, contain about sixty percent of a hexagonal phase similar to that previously proposed for the mineral, but also contain cubic structures similar to those of magnetite, Fe_3O_4, and a disordered form of wüstite, FeO.

The molecules of the protein ferritin, important for the transport of iron in the bodies of most living entities, from bacteria to humans, consist of a spherical shell of protein with an iron-rich core. The iron-rich cores were said to have the same structure as the ferrihydrite mineral, and high-resolution electron micrographs appeared to confirm the presence of the hexagonal 6LFh phase [77]. Nanodiffraction in a STEM instrument,

however, showed that, as in the ferrihydrite mineral, a variety of phases is present (see Fig. 7) with much the same phases as in the mineral, but in appreciably different proportions, varying with the origins of the ferritin [59].

6.2. Nanotubes and Nanoshells

Since the time of their discovery by Iijima [78] carbon nanotubes have been studied extensively for both their intrinsic interest as representing a new form of matter, and their potential industrial applications. The determinations of their detailed structures have been made mostly by use of high resolution TEM and by selected-area electron diffraction (SAED). However, the use of STEM instruments offers advantages for these purposes The SAED patterns are weak because they come from areas of much larger diameter than the tube diameters and usually depend on having long straight tubes of uniform structure, but STEM nanodiffraction patterns, given with incident beam diameters comparable with, or less than, the tube diameters, can be used to determine the structures of any small region of a tube, or of attachments or inclusions in a tube (see Fig. 8).

In a recent review [79], an account has been given of the results of bright-field and dark-field STEM imaging and individual nanodiffraction patterns or series of nanodiffraction patterns recorded in transit across a variety of nanotube and related systems. These techniques have contributed to our knowledge as follows.

Some multi-walled nanotubes do not have the circular cross-sections, universally assumed, but have cross-sections which are polygonal, and usually pentagonal.

The helix angles of the individual layers of carbon atoms in a multi-walled tube are not uniform, but tend to change at intervals of four or five layers.

The determination of the helix angles for single-walled nanotubes is quick and simple when nanodiffraction is used, so that statistics for the distributions of helix angles in various samples, or in local regions of any one sample may be accumulated readily.

In ropes of single-walled nanotubes, the helix angles may be uniform over regions 10 nm in diameter, but may vary slightly between such regions, giving rise to twists and bends of the ropes.

Multi-walled nanotubes and the associated near-spherical nanoshells, containing inclusions of metals or, usually, metal carbides, the crystallographic relationship between the nanotube walls and the inclusions gives evidence of the process of formation of these systems.

Similar structures have been found for nanotubes composed of the tungsten and molybdenum sulfides. Further applications of the nanodiffraction and STEM techniques have included studies of nanobelts such as those formed of ZnO and other oxides [80] and of boron and its carbides [81].

7. STUDIES OF CRYSTAL DEFECTS AND INTERFACES

The defects of crystals and the interfaces between differing crystal structures are of prime importance for the development of semiconductor and related components for

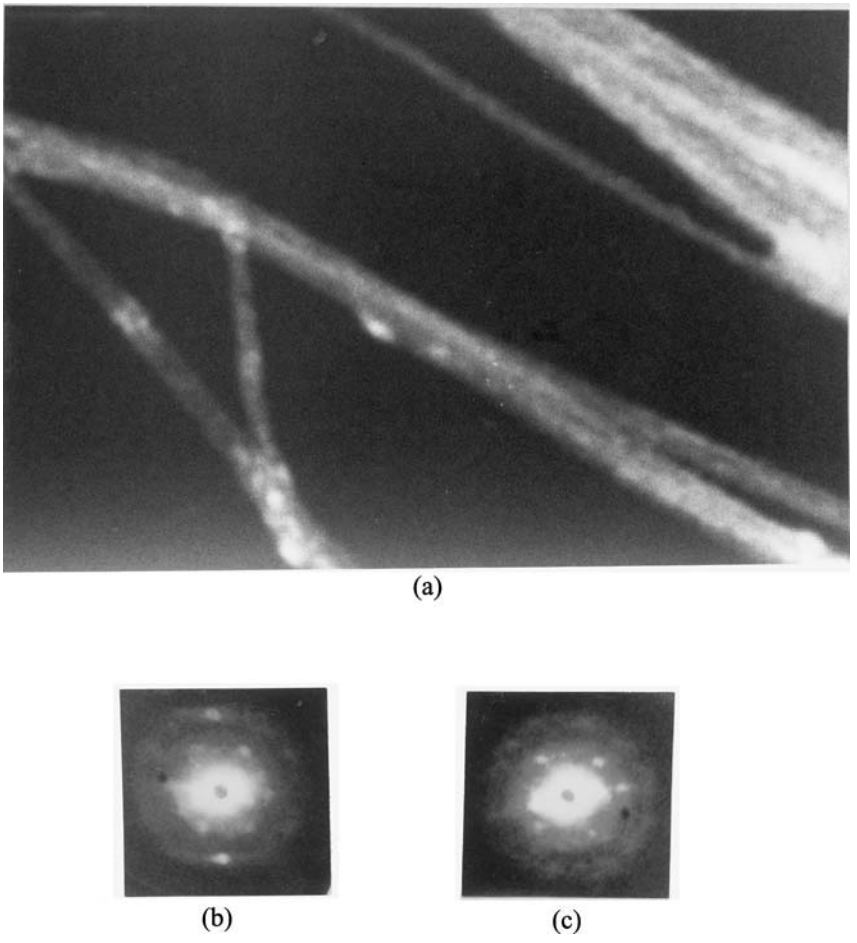

Figure 8. (a) A dark-field STEM image showing single-walled carbon nanotubes (SWnT) and bundles of SWnT, with nanocrystals of lead oxide attached. (b) Nanodiffraction pattern of SWnT, diameter 2 nm, helix angle 30 degrees and tilt 0. (c) Nanodiffraction pattern of SWnT, diameter 2 nm, helix angle 0, tilt 30 degrees.

the burgeoning micro-electronics industry. STEM imaging, particularly in the HAADF mode, is proving to be an important tool for their study. In common practice, a thin slice is cut to show a cross-section of the critical region of a device and the high-resolution image is obtained by viewing the slice along an axial direction of the crystal lattices involved.

For thin crystals, a detailed analysis of a defect may be possible. Planar defects have been seen in TEM images in diamond crystals [82]. Series of nanodiffraction patterns were obtained as a beam of 0.3 nm diameter was translated across such a defect at intervals of 0.02 nm. Comparison of the nanodiffraction pattern intensities

with dynamical diffraction calculations for various models showed best agreement with the Humble model [83].

It was shown by Pennycook *et al.* [84] that the high-resolution HAADF images obtained from reasonably thick crystals, and interfaces with their planes parallel to the electron beam, are in many case superior to those of HRTEM in that they do not suffer from the same complications of dynamical scattering effects which give strong variations of TEM contrast for variations of crystal thickness and orientation. Because the HAADF contrast arises from the incoherent addition of thermal diffuse scattering from all depths in the crystal, it may be considered, to a reasonable approximation, as being incoherent imaging, depending only on the number of atoms aligned in the beam direction.

The quasi-incoherent nature of the HAADF imaging of crystals aligned with the incident beam almost parallel with a principle crystal axis, has been confirmed by experiment and by theoretical analyses [85]. For such orientations, the channeling effect gives rise to an oscillation of the incident electron beam intensities and widths along the rows of atoms. As a consequence, there is some oscillatory component in the integrated intensity from the thermal diffuse scattering [26], but such oscillatory effects are relatively small and are rapidly damped with increasing thickness.

Because the electrons are channeled along the lines close to the atom rows, by excitation of the *1s* states of the potential wells of the rows of atoms, there is little spreading of the beams within the crystal and the intensity distribution at the exit face, and in the corresponding image, has clear maxima at the positions of the atomic rows, provided that the atomic rows are well separated. Figure 9 shows an image of the multiple interfaces of crystals of Si and Ge. The images of the separate atomic rows are clear within the individual crystal layers and at the boundaries [86].

Because the incident electron beam in a STEM instrument is not sharply defined, but has weak "tails" extending beyond the central intensity maximum, it is possible that some artefacts will arise. For example, weak maxima may appear in an image at positions close to atomic rows, where no atoms exist [87]. Also, when the rows of atoms are close together, the wavefields in the two potential wells may overlap, and the image intensities are affected. Recently, computer simulations have been made to evaluate these effects [88–91]. Similar, even more prominent and complicated effects of 'non-localization' appear in the corresponding HRTEM images. These effects are reduced when the resolution of the instrument is improved, for example by the use of systems for the correction of the objective lens aberrations.

8. THE STRUCTURE AND COMPOSITION OF SURFACES

8.1. Ultra-High Vacuum Instruments

Although the vacuum in the column of most dedicated STEM instruments is normally an order-of-magnitude better than that in most TEM instruments, it does not usually approach the ultra-high vacuum (UHV) level (better than 10^{-10} torr) considered necessary for the studies of surfaces which have been made for many years using the techniques of LEED (low-energy electron diffraction) or Auger analysis [92]. For some

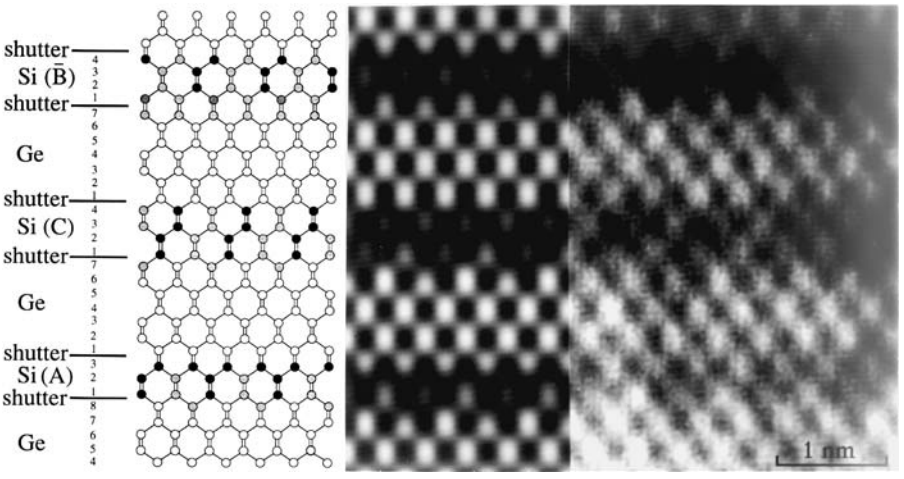

Figure 9. HAADF STEM image of a cross-section of a Si-Ge multilayer in <110> orientation, deposited in an MBE system with the shutter opened and closed at the indicated times to give the alternating Si and Ge layers, showing (left to right) a diagram of the structure, a simulated image and the observed image. [Courtesy of S. J. Pennycook,] c.f. [84].

materials, such as noble metals and oxides, having non-reactive surfaces, the vacuum of a normal STEM instrument may suffice, but for more general surface studies, special UHV instruments must be built [93, 94].

In the MIDAS instrument (a Microscope for the Imaging Diffraction and Analysis of Surfaces) the whole column is constructed of UHV-compatible components, a UHV specimen preparation and treatment chamber is attached and UHV is maintained throughout by the use of suitable ion pumps [93]. This instrument is equipped with the special devices needed for the imaging and analysis with low-energy secondary electrons and Auger electrons. The low-energy electrons emitted from the surfaces of a suitably biased specimen are detected or energy-analysed after they have been collected in the field-free spaces above or below the lens. In this way, high-resolution SEM or AEM images of the top and bottom surfaces of the specimen, and Auger analyses of the composition of the surfaces may be made and compared with the bright-field transmission image.

This instrument has been used for various studies of the initial stages of crystal growth on surfaces, including the nucleation and growth of crystallites of Ge on Si [94]. The image resolution is superior to that of existing UHV SEM instruments or AEM instruments and the possibility of correlating the images with those from STEM imaging modes and nanodiffraction adds greatly to its power and versatility.

8.2. Reflection Electron Microscopy

The technique of reflection electron microscopy (REM) has been widely developed and applied in many studies of the structure of crystals surfaces and of thin layers or deposits on surfaces [95, 96]. Applications of the technique using TEM instruments

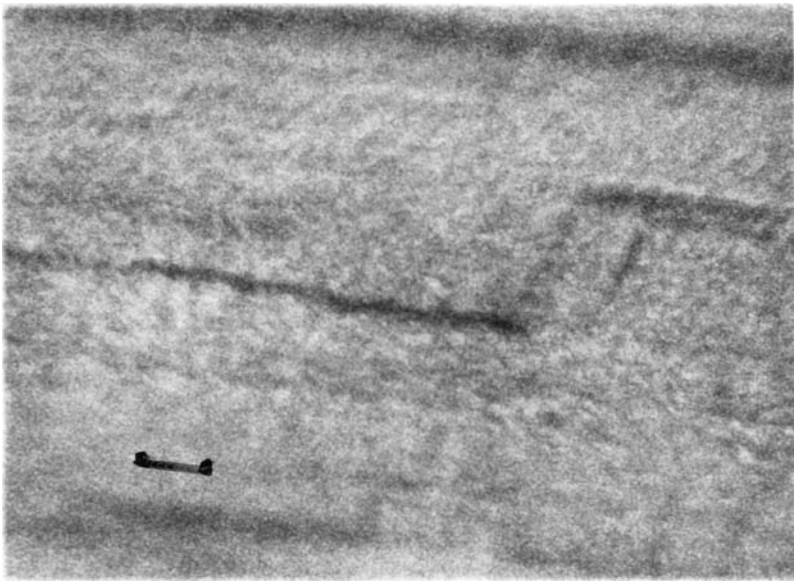

Figure 10. Scanning reflection electron microscopy (SREM) image of the surface of a crystal of MgO, obtained with the specular (400) reflection, showing surface steps [98]. Marker = 10 nm.

with grazing angles of incidence are normally limited by the relatively poor vacuum levels, but REM in special UHV instruments has allowed important studies of the structures, growth and interactions of steps and superlattices on semiconductor and other surfaces [97].

The equivalent scanning reflection electron microscopy (SREM) technique is possible with STEM instruments, using equivalent geometries. Figure 10, for example, is a SREM image showing atom-high steps on the surface of a crystal of MgO [98]. Also superlattice structures on crystal surfaces may be directly imaged [99], and surface reactions, such as the oxidation of copper, have been studied [100].

The advantage of SREM over REM is that the imaging may readily be combined with the observation of nanodiffraction patterns or EELS or X-ray microanalysis of small surface regions or of small protrusions from the surface. For example, nanodiiffraction patterns from crystallites of palladium, a few nm in diameter, sitting on the surface of MgO crystals showed their partial and progressive oxidation to PdO [101]. The special imaging modes developed for STEM may be applied for SREM. When a HAADF detector is used, the image of a surface depends very little on the crystal structure, but shows more clearly the surface topography [101].

The intensities of RHEED patterns and the contrast in REM or SREM images may be calculated by use of modified computer programs adapted from those originally developed for LEED [92, 102] or for TEM [21]. The multislice programs, used for transmission diffraction or for HRTEM, may be applied if the slices are taken perpendicular to the surface. Since the slice content is essentially non-periodic, a

periodic-continuation approximation is made with the vacuum and topmost crystal atomic layers repeated at large intervals [103, 104]. For SREM, the localized amplitude of the incident beam is used for the input, and the progressive penetration of the wave into the surface and its interaction with any perturbation of the surface structure can be followed.

8.3. Surface Channeling Effects

Calculations made using the multislice computer programs have revealed that, for certain diffraction geometries involved in REM or SREM, the penetration of the incident beam into the surface of a perfect crystal may be very small [105].

A surface-channeling phenomenon takes place, in which the electron wave is confined to just the first one or two atomic layers. The necessary condition is that a strong diffraction beam is generated in a direction parallel to the plane of the surface. Under these conditions, the specular reflection in the RHEED pattern becomes very strong, and the whole RHEED pattern, including the background of Kikuchi lines, is enhanced [106, 107].

With surface channeling, the REM or SREM image contrast is highly sensitive to small perturbations of the surface structure and the EELS analysis of the diffracted beams can be highly sensitive to the composition of the top surface layers [108].

8.4. MEED and MEEM

The severe fore-shortening of REM and SREM images may be avoided, to some extent, if the angles of diffraction by the surface planes are increased by decreasing the beam voltage and so increasing the wavelength. A number of medium-energy instruments operating in the range of 5 to 20 keV have been constructed for diffraction (MEED) and scanning microscopy (MEEM) [8–10]. With the simpler electron optics and the more compact design possible for this energy range, it was easier to produce systems operating in UHV with adequate provision for the preparation and treatment of clean surfaces.

With a cold field-emission electron source, operating in the same UHV environment, a relatively simple electron lens system can give image resolutions of a few nm. The diffraction pattern can be observed on a spherically curved fluorescent screen with energy-filtering meshes, as used for LEED, and a hole in the screen allows selected diffracted beams to be transmitted to a detector.

Such instruments have been applied to studies of the oxidation of copper surfaces [109] and for numerous studies of the surface structure and modifications of semiconductors and related materials.

9. AMORPHOUS MATERIALS

9.1. Thin Quasi-Amorphous Films

For a wide range of materials, including most biological materials, there is no periodic structure. Some local ordering often occurs on a nanometer scale, but in the absence

of long-range order, the diffraction patterns obtained by X-ray diffraction or SAED techniques show only a few diffuse haloes, and the materials are considered to be "amorphous". However, with STEM imaging and nanodiffraction, the local ordering may usefully be detected and measured. For the organic and biological materials, such studies are usually limited by their great susceptibility to radiation damage by the incident electron beam, but important progress has been made with investigations of thin films of many inorganic materials.

When a STEM beam of nanometer diameter passes through a thin film of quasi-amorphous material, the nanodiffraction pattern does not contain the diffuse haloes of normal SAED patterns, but shows a two-dimensional array of diffuse maxima and minima, corresponding to the local ordering of the atoms within the illuminated area of the specimen. The patterns change as the beam is moved over distances of the order of 1 nm, and different arrays of atoms are illuminated. Assuming that, for very thin films, the scattering can be interpreted in terms of the simple kinematical approximation, it should, in principle be possible to derive some information about the arrangement of the atoms within each illuminated area. It has been considered that, from the observation of many such patterns, it should be possible to derive not only the average pair-wise, atom-to-atom distances, as in the case of SAED patterns [110], but also the presence of many-atom configurations, or medium-range order [111].

It has been shown by Treacy and Gibson [112] that the technique of TEM with a hollow-cone (or gyrating beam) illumination may form the basis for 'variable-coherence' microscopy, or 'fluctuation microscopy'. By observation of the variation of the speckle in the dark-field images of thin amorphous films, the degree of medium range order present may be investigated. In such a way, they derived information of the extended correlations in semiconductor films [113]. These authors suggested that the reciprocity principle implied that TADDF STEM images using a thin annular detector, could give the same information. An analysis of the equivalent STEM technique was given by Cowley [114], who pointed out that several possible, and experimentally simpler, approaches are possible if the STEM methods are combined with nanodiffraction observations.

9.2. Thick Amorphous Films

For many biological samples, such as those containing complete cells, and for specimens held in environmental cells with controlled atmospheres, it is desirable to obtain images of specimens which may be several micrometers thick. To achieve the required increase in penetration, high-voltage TEM instruments, operating at 1 MeV or more, have been employed, in spite of the large and expensive installations required. However, it has been shown that, for the same voltages, the effective penetration should be greater for STEM and several attempts have been made to build high-voltage STEM instruments operating at up to 1 MeV.

The loss of resolution for thick specimens derives from two causes. Because of multiple elastic scattering in the specimen, there is uncertainty in the position of scattering of any given electron so that the location of any scattering object becomes

uncertain. Also, for a thick object there can be multiple energy losses of the electrons, with an energy loss of about 25 eV, on the average, for each event, and the chromatic aberration of the imaging system in TEM gives a spread of the image. For STEM, the first of these causes for resolution loss applies, but the second does not apply because the main imaging components come before the specimen. For typical specimens, the electron energy needed for a given penetration is reduced by a factor of at least 2 for STEM, or the resolution for a given electron energy may be improved by an equal factor [115, 116]. Observations made using the high-voltage STEM instrument built by Strojnik, [7] have confirmed these estimates.

For specimens held in environmental cells, the path length of the electrons in a scattering medium, including the gas in the cell, is greater and the first of the above resolution-impairing factors is more important. The advantage of the STEM system over the TEM is then not so great.

10. STEM HOLOGRAPHY

10.1. Gabor's in-line Holography

In his original proposal for holography, Gabor [117] suggested that the deleterious effects of lens aberrations on electron microscopy could be overcome by reconstructing the object wave from a hologram in which the wave scattered by the object is made to interfere with a reference wave. He proposed a scheme suitable for use with very thin specimens or specimens for which the object of interest covers only a small part of the image field. A small probe formed by imaging a small bright source with the strong objective lens, as in a STEM instrument, is focused close to the specimen, as suggested in Fig. 3. The greatly enlarged, out-of-focus shadow image is then the hologram, containing the interference effects of the transmitted wave, acting as a reference, and the waves scattered by the object. In the course of reconstruction of the object wave, compensation can be made for the phase distortions due to the aberrations of the objective lens by using either an optical system, as suggested by Gabor, or by the computerized manipulation of a digitized hologram [118].

A demonstration of this form of in-line holography has been given, with relatively low resolution, with reconstruction from a defocused shadow image in a STEM instrument [119]. However, because the phases of the waves are lost in the recording of the intensity distribution in the hologram, the reconstructed image is always accompanied by a defocused conjugate image. Various schemes have been proposed whereby this conjugate image may be made negligibly small or eliminated. By recording the hologram very far out-of-focus, the conjugate image may be made very diffuse so that it forms only a weakly-modulated background; or it may be removed, in principle, if a series of holograms is recorded with small translations of the incident beam [120].

A further limitation of in-line holography is that the reconstruction from the intensity distribution may contain terms of second and higher order in the scattering function of the object. These terms are avoided only if the scattering by the object is very weak compared with the reference wave so that only first-order interference terms

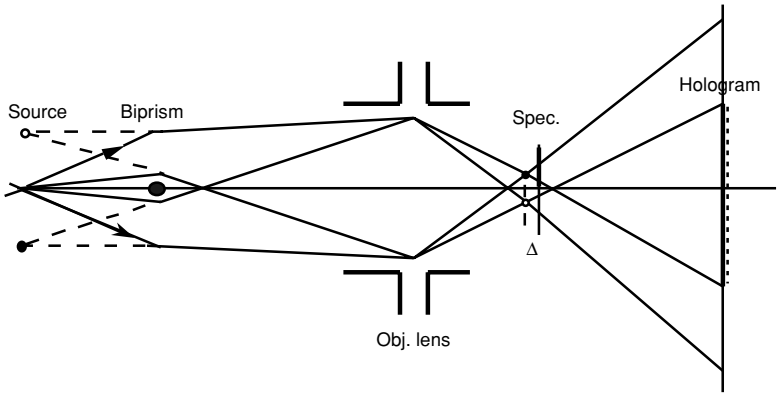

Figure 11. Diagram of the arrangement for off-axis electron holography in a STEM instrument. A biprism in the illuminating system gives two small probes near the specimen, one passing through the specimen and one through vacuum.

are significant. Thus in-line holography can, in practice, be applied only to very thin specimens of light-atom material.

10.2. Off-Axis Holography

The major advances in electron holography have come from the use of off-axis holography in which the reference wave has passed only through vacuum and is made to interfere with the wave passing through the specimen after the two waves have been deflected by an electrostatic biprism placed in the imaging system. This form of electron holography has been widely used for the enhancement of image resolution, for the mapping of weak electrical and magnetic fields, within and around solids and for other purposes [121, 122].

It has been pointed out that many forms of electron holography are possible, and that, as suggested by the reciprocity principle, for each form of holography applicable in a TEM instrument, there is a STEM equivalent [123]. In the STEM equivalent of the off-axis form illustrated in Fig. 11, an electrostatic biprism is placed in the illuminating system of the instrument so that two focused probes are formed by the objective lens in the specimen plane, and these are scanned in parallel, one through the specimen and one through vacuum, to record the hologram.

Little use has been made, as yet, of the off-axis form of STEM holography for the enhancement of resolution, but the technique has proved highly effective for the study of magnetic fields in and around ferromagnetic objects [124]. Figure 12, for example, shows a display of the contoured field strength in a thin film of Co. [125]. The spatial resolution for such images can be about 1 nm, which is adequate for most purposes. Applications of this technique have been made to the study of the configurations of magnetic domains within small crystals and the fields within multi-layer composites of ferromagnetic and non-ferromagnetic materials [126].

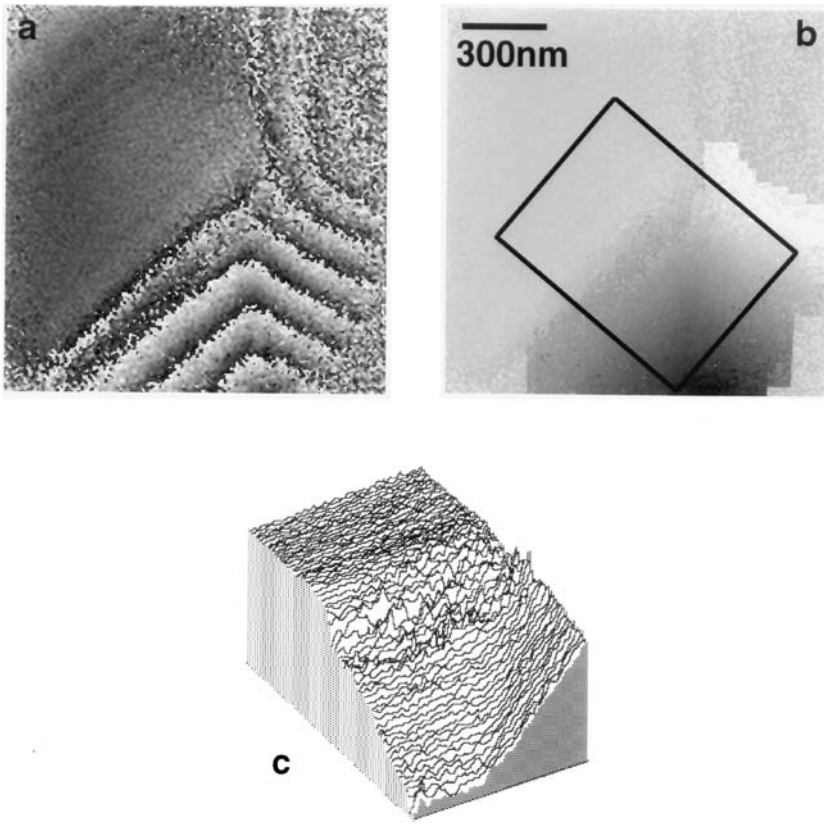

Figure 12. Determination of the magnetization in a 20 nm Co film using STEM holography. (a) Wrapped phase image. (b) Partially unwrapped phase image. (c) Three-dimensional view of the region marked in (b); the gradient of the phase difference taken perpendicular to the edge determines the absolute value of the magnetization [125].

11. ULTRA-HIGH-RESOLUTION STEM

11.1. Atomic Focusers

As pointed out in our discussion of the STEM imaging of crystals, above, the passage of an incident STEM beam along a row of atoms in a thin crystal can produce a cross-over near the exit face having a diameter of 0.05 nm or less. If this fine probe can be scanned over a thin specimen, STEM imaging with a correspondingly high resolution should be possible [54, 55]. Because the effective focal length of such an "atomic-focuser" lens is of the order of 2 nm, there are severe practical difficulties in realizing this STEM mode with the atomic-focuser crystal and the specimen so close together.

If the distance between the atomic-focuser crystal and the specimen is increased to, perhaps, 100 nm, the arrangement is that for in-line electron holography. The area of the specimen illuminated at any time has a diameter of about 10 nm and no scanning of the beam is needed to produce a useful image. Computer simulations have shown that the resolution attainable in the image reconstructions from such an arrangement may be better than 0.05 nm when a thin gold crystal is used as the focuser [127]. The conjugate image is defocused by an amount equal to twice the separation of the crystals and so forms only a very diffuse background.

Further schemes for attaining ultra-high resolution in a STEM instrument depend on the formation of a periodic, coherent array of fine cross-overs at the exit face of a thin 'atomic-focuser' crystal, and the formation of Fourier images at regular intervals in the subsequent space [21]. An experimental realization of one such scheme has been shown with a STEM beam focused on one wall of a carbon nanoshell to image the opposite wall [53]. The resolution observed in these experiments was approximately equal to 0.06 nm, the diameter of the nanoprobe formed by a graphite crystal.

11.2. Aberration Correction

In recent years, considerable progress has been made in the attempts to correct the aberrations of the objective lens used for TEM and STEM by the addition of systems of multipole auxiliary lenses, following suggestions by Scherzer [128], Rose [129] and Crewe [130]. For STEM, a quadrupole-octupole aberration corrector has been shown to be effective [15]. The third-order spherical aberration constant may be reduced to zero, or to some controlled small value. The resolution limit possible for STEM imaging is thereby reduced from about 0.2 nm to better than 0.1 nm. As shown in Fig. 13, the correction of aberrations of the objective lens of a STEM instrument gives considerable improvement in definition, contrast and signal-to-noise ration for the imaging of individual heavy atoms on a light-atom support [131].

Such resolution improvement is often demonstrated by images of thin crystals of silicon in [110] orientation. In this projection, there are pairs of atom rows with a separation of 0.136 nm, giving the so-called "silicon dumb-bells" in images with sufficient resolution. A more important feature of the improved resolution attainable with the aberration correction is the improvement of the localization in the images of crystals. There is less cross-talk between images of adjacent rows of atoms, and the positions of atom rows in asymmetrical surroundings, as at boundaries or interfaces are more accurately indicated [16].

11.3. Combining Nanodiffraction and Imaging

For normal STEM imaging, only one signal is derived, either from the incident beam spot or from all or parts of the diffraction pattern, to form the image. It has long been realized that it should be possible to take advantage of the fact that for each incident beam position a complete two-dimensional nanodiffraction pattern can, in principle, be recorded, and this should allow one to derive much more information, and possibly much better resolution, than that from the standard techniques.

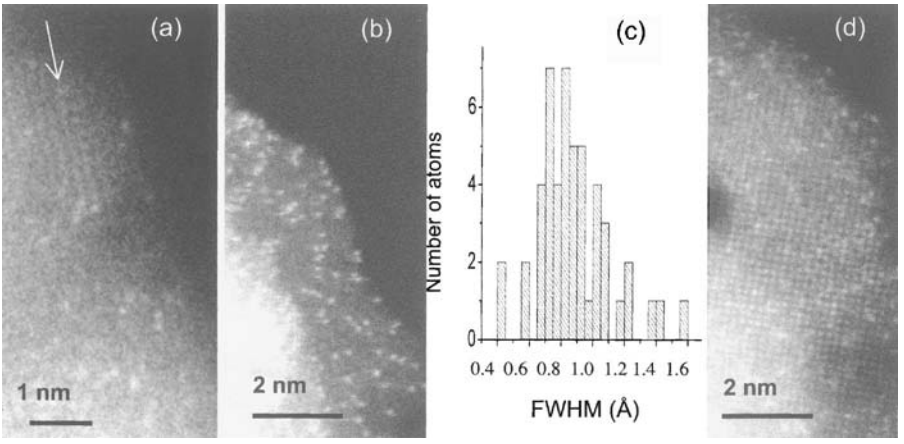

Figure 13. Images of individual La atoms on γ-alumina obtained with a 300 kV STEM, before (a) and after (b, d) aberration correction, showing the improvement in contrast, resolution and signal-to-noise ratio. In (d), the La atoms are visible at the same time as the γ-Al_2O_3 lattice in [100] orientation. The histogram (c) shows the FWHM of intensity profiles. (Courtesy of Dr. S. J. Pennycook], [131]

In a scheme proposed by Konnert *et al.* [132], the nanodiffraction patterns are recorded for a series of closely-spaced positions of the incident beam. Fourier transform of the nanodiffraction pattern intensity distributions gives a series of correlated real-space autocorrelation functions from which the structure of the specimen can be derived. This process was carried out for a thin crystal of silicon in [110] orientation using a STEM instrument having a resolution of about 0.3 nm and gave a calculated image having a resolution which was clearly better than 0.1 nm.

In a formulation of the problem by Rodenburg and Bates [133], a four-dimensional intensity function is derived with the two dimensions of the image and two dimensions of the nanodiffraction intensity distributions. It was shown that, by taking a particular two-dimensional section of this four-dimensional function, an image may be derived with an improvement of resolution by at least a factor of two. The validity of this approach was demonstrated by light-optical analogue experiments and by STEM experiments with moderate resolutions [134]. The theoretical treatment of this procedure shows that the perturbations of the phase distributions in the transfer function of the objective lens due to the lens aberrations are cancelled out, and the resolution obtainable should be twice as good as that corresponding to the objective aperture size, which can, in principle, be arbitrarily large [135]. The practical limitations on resolution enhancement then come from the incoherent limiting factors of microscope instabilities. In experimental tests of the method, made for simplicity on a one-dimensional object, the side of a multi-wall carbon nanotube, a resolution of better than 0.1 nm was demonstrated using a STEM instrument for which the resolution for normal STEM imaging is about 0.3 nm [136].

One limitation of the Rodenburg scheme is that it is applicable only to thin, weakly scattering objects since there are background contributions to the derived

image arising from a defocused conjugate image and second- and higher-order terms in the scattering function, as in in-line holography. Also there is the practical problem that an enormous amount of data-recording and computation is involved in the derivation and treatment of the four-dimensional intensity function, requiring long exposure times for reasonable specimen areas. It has been suggested [137] that the first of these difficulties may be avoided if the scheme is combined with off-axis holography, making use of an electrostatic biprism to produce two focussed probes in the STEM instrument (Fig. 11). The second difficulty may be avoided if the required two-dimensional section of the four-dimensional function is automatically produced during the recording process by scanning the two probes in opposite directions, which is possible if the voltages on two perpendicular biprisms are scanned [138].

12. CONCLUSIONS

In this review, it has been shown that STEM imaging, particularly when accompanied by the associated techniques of nanodiffraction and the microanalysis of nanometer-sized regions, has the potential for being of increasing value for studies of fundamental importance for nanotechnology. The dedicated STEM instrument with a cold-field-emission gun offers the highest available intensity in a probe of nanometer diameter or less and thus ensures the greatest capability for studies of the shapes, sizes, crystal structures, surface structures and compositions of nanometer-size regions of small particles, thin films and nanocrystals.

As in TEM, the specimens needed for STEM imaging or nanodiffraction or microanalysis must usually be very thin with thicknesses less than few hundred nm. Nanoparticles may be supported on very thin supporting films, usually of amorphous carbon, or else, in favorable cases, they may be self-supporting as is usually true for nanotubes and nanowires. For the studies of three dimensional structures such as the components of microcircuitry, it is necessary to cut thin sections. Efficient procedures have been developed for this purpose [139]. Adaptation of the STEM instrumentation for surface studies allows the imaging, diffraction and analysis of the surfaces of bulk materials, with high-resolution SEM and AEM for general morphological studies and, in the case of flat crystals surfaces, SREM and associated nanodiffraction and microanalysis.

Further developments of the STEM techniques are to be anticipated. Because the number of dedicated STEM instruments is much smaller than the number of TEM instruments, and the number of investigators concerned with the development of new methods for their use is correspondingly limited, many possibilities remain to be explored. The excitement associated with the recent development of the techniques for ultra-high resolution may well prompt new attempts to explore further the new and existing capabilities.

The measurement and quantitative interpretation of STEM image intensities is being pursued in some limited cases, such as for the HAADF images of crystals of simple structure and their interfaces, and work has commenced on the theoretical basis for detailed interpretations [140, 141].

There have been some measurements of image intensities from thin crystals as adjuncts to the structure analysis of crystals by electron diffraction methods [142], but these measurements have been confined to TEM and SAED techniques. The corresponding measurements with STEM and nanodiffraction, applicable to much smaller regions of crystallites and crystal defects, or to nanoparticles, are missing. There have been indications that nanodiffraction, combined with STEM imaging, may be used to explore the arrangements of atoms, and the local symmetries, within the unit cells of complex structures [143], but this possibility has not been pursued much further.

A few of the possibilities for coherent nanodiffraction in STEM instruments have been explored to a limited extent, as outlined above. There have been some limited observations but few quantitative measurements. Much more remains to be done before the wealth of potential applications in nanotechnology and nanoscience can be fully exploited.

ACKNOWLEDGEMENTS

The author is grateful to the many students, post-docs and collaborators who have contributed to the exploration of the STEM techniques over the past twenty five years or so in this laboratory; to the Center for High Resolution Electron Microscopy at ASU for provision of the instruments and facilities; and to the staff of the Center, particularly Al Higgs, John Wheatley and Karl Weiss, for their continued support and help in the essential task of keeping the instruments running. Many thanks to Dr. Stephen Pennycook for providing figures 9 and 13.

REFERENCES

1. M. von Ardenne, *Z. Phys.*, 109 (1938) 553.
2. A. V. Crewe and J. Wall, J. Mol. Biol., 48 (1970) 373.
3. A. V. Crewe, J. Wall and J. Langmore, *Science*, 168 (1970) 1333.
4. J. M. Cowley, *Micros. Res. Tech.*, 46 (1999) 75.
5. J. M. Cowley, *Appl. Phys. Letts.*, 15 (1969) 58.
6. E. Zeitler and M. G. R. Thompson, *Optik* 31(1970), 258 and 359.
7. A. Strojnik, *Scanning Electron Microscopy/1981/1*, SEM Inc., AMF O'Hare (Chicago) Om Johari, Ed., (1981), 117 and 122.
8. C. Elibol, H.-J. Ou, G. G. Hembree and J. M. Cowley, *Rev. Sci. Instrum.*, 56 (1985) 1215.
9. J. A. Venables, A. P. Janssen, P. Akhter, J. Derrien and C. J. Harland, *J. Micros.*, 118 (1980) 351.
10. M. Ichikawa, T. Doi, M. Ichihashi and K. Hayakawa, *Jpn. J. Appl. Phys.*, 23 (1984) 913.
11. E. M. James and N. D. Browning, *Ultramicroscopy*, 78 (1999) 125.
12. N. D. Browning, L. Arslan, P. Moeck and T. Topuria, *phys. stat. sol (b)*, 227 (2001) 229.
13. Y. Hirotsu, M. Ishimaru, T. Ohkubo, T. Hanada and M. Sugiyama, *J. Electron Micros.*, 50 (2001) 435.
14. P. E. Batson, N. Dellby and O. L. Krivanek, *Nature*, 418 (2002) 617.
15. O. L. Krivanek, N. Dellby, M. F. Murfit, P. D. Nellist and Z. Szilagyi, *Micros. Microanal.* (In Press).
16. J. M. Cowley and M. M. Disko, *Ultramicroscopy*, 5 (1980) 469.
17. R. W. Carpenter and J. C. H. Spence, *J. Microsc.*, 142 (1986) 211.
18. V. Ronchi, *Appl. Optics*, 3 (1964) 437.
19. J. M. Cowley, *Ultramicroscopy*, 7 (1981) 19.
20. J. A. Lin and J. M. Cowley, *Ultramicroscopy*, 19 (1986) 31.
21. J. M. Cowley, *Diffraction Physics (3rd revised edition)*, Elsevier Science B.V., Amsterdam, The Netherlands (1995).
22. J. M. Cowley and A. Y. Au, in *Scanning Electron Microscopy, 1978, Vol. 1*, Om Johari, Ed., SEM Inc., Illinois, (1978) 53.

23. J. Liu and J. M. Cowley, *Ultramicroscopy*, 52 (1993) 335.
24. A. Howie, *J. Microscopy*, 117 (1979) 11.
25. Z. L. Wang and J. M. Cowley, *Ultramicroscopy*, 31 (1989) 437.
26. S. Hillyard and J. Silcox, *Ultramicroscopy*, 52 (1993) 325.
27. R.-J. Liu and J. M. Cowley, *J. Micros. Soc. Amer.*, 2 (1996) 9.
28. J. M. Cowley, *J. Electron Micros.*, 50 (2001) 147.
29. J. M. Cowley, V. I. Merkulov and J. S. Lannin, *Ultramicroscopy*, 65 (1996) 61.
30. J. M. Gibson and A. Howie, *Chem. Scripta*, 14 (1978) 109.
31. J. M. Chapman, P. E. Batson, E. M. Waddell and R. P. Ferrier, *Ultramicroscopy*, 3 (1978) 203.
32. J. C. H. Spence and J. M. Zuo, *Electron Microdiffraction*, Plenum Press, New York and London (1992).
33. M. Tanaka, M. Terauchi, K. Tsuda and K. Saitoh, *Convergent beam electron diffraction, IV*, JEOL Ltd., (2002).
34. W. Hoppe, *Ultramicroscopy*, 10 (1982) 187.
35. B. C. McCallum and J. M. Rodenburg, *Ultramicroscopy*, 52 (1993) 85.
36. J. C. H. Spence and J. M. Cowley, *Optik*, 50 (1978) 129.
37. J. M. Cowley, *Chem. Scripta*, 14 (1978–79) 279.
38. J. C. H. Spence, *Acta Cryst. A*, 54 (1998) 7.
39. A. E. C. Spargo, M. Beeching and L. J. Allen, *Ultramicroscopy*, 55 (1994) 329.
40. J. M. Cowley and A. F. Moodie, *Acta Cryst.*, 10 (1957) 609.
41. P. Goodman and A. F. Moodie, *Acta Cryst.*, *A*, 30 (1974) 280.
42. K. Ishizuka and N. Uyeda, *Acta Cryst. A.*, 33 (1977) 740.
43. H. A. Bethe, *Ann. Physik.*, 87 (1928) 55.
44. P. B. Hirsch, A. Howie, R. B. Nicholson, D. W. Pashley and M. J. Whelan, *Electron Microscopy of Thin Crystals*, Butterworth and Co. London (1965).
45. C. J. Humphreys and E. G. Bithel, in *Electron Diffraction Techniques, Vol.1*, J. M. Cowley, Ed., Oxford Univ. Press, Oxford. (1992).
46. J. Barry, in *Electron Diffraction Techniques, Vol. 1*, J. M. Cowley, Ed., Oxford Univ. Press, Oxford (1992).
47. K. Ishizuka, *Ultramicroscopy*, 90 (2002) 71.
48. Z. L. Wang, *Elastic and Inelastic Scattering in Electron Diffraction and Imaging*, Plenum Press, New York, (1995).
49. P. Rez. *Ultramicroscopy*, 81 (2000) 195.
50. D. Van Dyck and M. Op de Beeck, *Ultramicroscopy*, 64 (1996) 99.
51. S. J. Pennycook, *Advances in Imaging and Electron Physics*, 123 (2002) 173.
52. M. Sanchez and J. M. Cowley, *Ultramicroscopy*, 72 (1998) 213.
53. J. M. Cowley and J. B. Hudis, *Micros. Microanal.*, 6 (2000) 429.
54. V. V. Smirnov, *J. Phys. D*, 31 (1998) 1548.
55. J. M. Cowley, J. C. H. Spence and V. V. Smirnov, *Ultramicroscopy*, 68 (1997) 135.
56. J. M. Cowley, R. E. Dunin-Borkowski and M. Hayward, *Ultramicroscopy*, 72 (1998) 223.
57. R. E. Dunin-Borkowski and J. M. Cowley, *Acta Cryst. A*, 55 (1999) 119.
58. J. M. Zuo, I. Vartanyants, M. Gao, R. Zhang and L. A. Nagahara, *Science* (2003) (In press).
59. J. M. Cowley, D. E. Janney, R. C. Gerkin and P. R. Buseck, *J. Struct. Biol*, 131 (2000) 210.
60. J. M. Zuo, M. Kim, M. O'Keeffe and J. C. H. Spence, *Nature*, 401 (1999) 49.
61. J. M. Cowley and J. C. H. Spence, *Ultramicroscopy*, 6 (1981) 359.
62. M. Pan, J. M. Cowley and J. C. Barry, *Ultramicrsocopy*, 30 (1989) 385.
63. J. Zhu and J. M. Cowley, *Acta Cryst. A*, 38 (1982) 718.
64. J. Zhu, H. Q. Ye and J. M. Cowley, *Ultramicroscopy*, 18 (1985) 111.
65. J. Zhu and J. M. Cowley, *J. Appl. Cryst.*, 16 (1983) 171.
66. R. F. Egerton, *Electron Energy Loss Spectroscopy*, Plenum Press, New York (1986).
67. H. Raether, *Excitation of Plasmons and Interband Transitions by Electrons*, Springer-Verlag, Berlin (1980).
68. M. R. Scheinfein, J. S. Drucker and J. K. Weiss, *Phys. Rev. B*, 47 (1993) 4068.
69. G. G. Hembree, P. A. Crozier, J. S. Drucker, M. Krishnamurthy, J. A. Venables and J. M. Cowley, *Ultramicroscopy*, 31 (1989) 111.
70. M. Pan, J. M. Cowley and I. Y. Chan, *J. Appl. Cryst.*, 20 (1987) 300.
71. J. M. Cowley and R. J. Plano, *J. Catalysis*, 108 (1987) 199.
72. J. A. Allpress and J. V. Sanders, *Surf. Sci.*, 7 (1965) 1.
73. J. M. Cowley and R. A. Roy, in *Scanning Electron Microscopy/1981*, Om Johari, Ed., SEM Inc., AMF O'Hare, (Chicago), (1982) 143.
74. V. A. Drits, B. A. Sakharov, A. L. Salyn and A, Manceau, *Clay Minerals*, 28 (1993) 185.

75. D. E. Janney, J. M. Cowley and P. R. Buseck, *Amer. Mineral.*, 85 (2000) 1180.
76. D. E. Janney, J. M. Cowley and P. R. Buseck, *Amer. Mineral.*, 86 (2001) 327.
77. W. H. Massover and J. M. Cowley, *Proc. Nat. Acad. Science*, 70 (1973) 3847.
78. S. Iijima, *Nature*, 354 (1991) 56.
79. J. M. Cowley, in *Electron Microscopy of Nanotubes and Nanowires*, Ed. Z. L. Wang, Kluwer Academic/Plenum Publishers (2003).
80. Z. W. Pan, Z. R. Dai and Z. L. Wang, *Science*, 291 (2001) 1947.
81. C. Jones Otten, O. R. Lourie, M.-F. Yu, J. M. Cowley, M. J. Dyer, R. F. Rouff and W. E. Buhro, *J. Amer. Chem. Soc.*, 124 (2002) 4564.
82. P. Humble, *Proc. Roy, Soc. London*, A381 (1982), 65.
83. Cowley, J. M., Osman, M. A. and Humble, P., *Ultramicroscopy*, 15 (1984) 311.
84. S. J. Pennycook and D. E. Jesson, *Ultramicroscopy*, 37 (1991) 14.
85. P. D. Nellist and S. J. Pennycook, *Ultramicroscopy*, 78 (1999) 111.
86. B. Rafferty, P. D. Nellist and S. J. Pennycook, *J. Electron Micros.*, 50 (2001) 227.
87. K. Watanabe, N. Nakanishi, T. Yamazaki, M. Kawasaki, I. Hashimoto and M. Shiojiri, *phys. stat. solidi, (b)*, 235 (2003) 179.
88. G. R. Anstis, D. Q. Cai and D. J. H. Cockayne, *Ultramicroscopy*, 94 (2003) 309.
89. C. Dwyer and J. Etheridge, *Ultramicroscopy* (In press).
90. P. M. Voyles, J. L. Grazul and D. A. Muller, *Ultramicroscopy* (In press).
91. Z. Yu, P. E. Batson and J. Silcox, *Ultramicroscopy* (In press).
92. J. B. Pendry, *Low Energy Electron Diffraction*, Academic Press, New York, London (1974).
93. J. A. Venables, *Introduction To Surface and Thin Film Processes*, Cambridge University Press, UK, (2000).
94. M. Krishnamurthy, J. S. Drucker and J. A. Venables, *J. Appl. Phys.*, 69 (1991) 6461.
95. J. M. Cowley, in *Handbook of Microscopy, Vol.1, Methods 1*, Eds., S Amelinckx, D. Van Dyck, J. F. Van Landuyt, and G. Van Tenderloo, VCH Verlag, Weinheim, Germany (1997).
96. K. Yagi in *Electron Diffraction Techniques, Vol. 2*, J. M. Cowley, Ed., Oxford Univ. Press, Oxford, (1993) 260.
97. Y. Tanishiro, K. Takayanagi and K. Yagi, *J. Microsc.*, 142 (1986) 211.
98. J. M. Cowley, *Ultramicroscopy*, 27 (1989) 319.
99. J. Liu and J. M. Cowley, *Ultramicroscopy*, 48 (1993) 381.
100. Milne, R. H., in *Reflection High Energy Electron Diffraction*, Eds. P. K. Larson, P. J. Dobson, Plenum Press, New York and London (1988), p. 317.
101. H.-J. Ou and J. M. Cowley, *phys. stat. solidi* (*a*), 107 (1988) 719.
102. J. M. McCoy and P. A. Maksym, *Surface Sci.*, 310 (1994) 217.
103. L. M. Peng and J. M. Cowley, *Acta Crystallog.*, *A*, 42 (1986) 552.
104. Y. Ma and L. D. Marks, *Micros. Res. Tech*, 20 (1992) 371.
105. Z. L. Wang, J. Liu, P. Lu and J. M. Cowley, *Ultramicroscopy*, 27 (1988) 101.
106. N. Yao and J. M. Cowley,*Ultramicroscopy*, 33 (1990) 237.
107. M. Gajdardziska-Josifoska and J. M. Cowley, *Acta Crystallog., A*, 47 (1991) 74.
108. Z. L. Wang and J. M. Cowley, *J. Micros. Spectros. Electroniques*, 13 (1988) 184.
109. J. D. Landry, G. G. Hembree, P. E. Hojlund-Nielsen and J. M. Cowley, in *Scanning Electron Microscopy, 1976/1.*, Om Johari, Ed., IITResearch Institute, Chicago, Ill., (1976), 239.
110. D. J. H. Cockayne, D. R. McKenzie, W. McBride, C. Goringe and D. McCullock, *Microsc. Microanal.* 6 (2000) 329.
111. J. M. Cowley in *Diffraction Studies of Non-Crystalline Substance*, I. Hargittai and W. J. Orville-Thomas, Eds., Elsevier Sci. Publ. (Amsterdam) (1981) 847.
112. M. M. J. Treacy and J. M. Gibson, *Acta Crystallog.*, *A*, 52 (1996) 212.
113. J. M. Gibson, M. M. J. Treacy and P. M. Voyles, *Ultramicroscopy*, 83 (2000) 169.
114. J. M. Cowley, *Ultramicroscopy*, 90 (2002) 197.
115. H. T. Pearce-Percy and J. M. Cowley, *Optik*, 44 (1976) 273.
116. D. J. Smith and J. M. Cowley, *Ultramicroscopy*, 1 (1975) 127.
117. D. Gabor *Nature*, 161 (1948) 777.
118. J. M. Cowley and D. J. Walker, *Ultramicroscopy*, 6 (1981) 71.
119. J. A. Lin and J. M. Cowley, *Ultramicroscopy*, 19 (1986) 31.
120. J. A. Lin and J. M. Cowley. *Ultramicroscopy*, 19 (1986) 179.
121. A. Tonomura, L. F. Allard, G. Pozzi, D. C. Joy and Y. A. Ono, Eds. *Electron Holography*, Elsevier, Amsterdam (1995).

122. E. Völkl, L. F. Allard and D. C. Joy, Eds., *Introduction to Electron Holography*, Kluwer Academic/Plenum Publ., New York, etc. (1998).
123. J. M. Cowley, *Ultramicroscopy*, 41 (1992) 335.
124. M. Mankos, M. R. Scheinfein and J. M. Cowley, *J. Appl. Phys.*, 75 (1994) 7418.
125. M. Mankos, A. A. Higgs, M. R. Scheinfein and J. M. Cowley, *Ultramicroscopy*, 58 (1995) 87.
126. M. Mankos, M. R. Scheinfein and J. M. Cowley, in *Advances in Imaging and Electron Physics*, P. Hawkes, Ed., 98 (1996) 323.
127. V. V. Smirnov and J. M. Cowley, *Phys. Rev. B.*, 65 (2002), 064109.
128. O. Scherzer, *Optik*, 2 (1947) 114.
129. H. Rose, *Ultramicroscopy*, 56 (1994) 11.
130. A. V. Crewe and N. W. Parker, *Optik*, 46 (1976) 183.
131. S. J. Pennycook, A. R. Lupini, M. Varela, A. Borisevich, Y. Peng and P. D. Nellist., *in AIP Conf. Proceedings*, *From the Atomic to the Nanoscale* (In press).
132. J. Konnert, P. D'Antonio, J. M. Cowley, A. Higgs and H. J. Ou, *Ultramicroscopy*, 30 (1989) 371.
133. J. M. Rodenburg and R. H. T. Bates, *Philos. Trans. Roy. Soc. Lond.*, A339 (1992) 521.
134. J. D. Rodenburg, B. C. McCallum and P. D. Nellist, *Ultramicroscopy*, 48 (1993) 304.
135. J. M. Cowley, *Ultramicroscopy*, 87 (2001) 1.
136. J. M. Cowley and J. Winterton, *Phys. Rev. Letts.*, 87 (2001) 016101.
137. J. M. Cowley, *Ultramicroscopy*, 96 (2003) 163.
138. J. M. Cowley, *Microsc. Microanal.* (In press).
139. R. Anderson, B. Tracy and J. Bravman, *MRS Proceedings* (1991) 254.
140. L. J. Allen, S. D. Findlay, M. P. Oxley and C. J. Rossouw, *Ultramicroscopy*, 96 (2003) 47.
141. S. D. Findlay, L. J. Allen, M. P. Oxley and C. J. Rossouw. *Ultramicroscopy*, 96 (2003) 65.
142. D. L. Dorset, *Structural Electron Crystallography*, Plenum Press, New York and London (1995).
143. H.-J. Ou and J. M. Cowley, in *Proc. 46th. Annual Meeting, Electron Micros. Soc Amer.*, G. W. Bailey, Ed., San Francisco Press, San Francisco (1988), 882.